Imaging northern Cascadia wave speed structure and slow slip

Carl W. Ulberg

A dissertation

submitted in partial fulfillment of the

requirements for the degree of

Doctor of Philosophy

University of Washington

2018

Reading Committee:

Kenneth C. Creager, Chair

Seth C. Moran

John E. Vidale

Program Authorized to Offer Degree:

Department of Earth and Space Sciences

University of Washington

Abstract

Imaging northern Cascadia wave speed structure and slow slip

Carl W. Ulberg

Chair of the Supervisory Committee:

Kenneth C. Creager

Department of Earth and Space Sciences

I calculate tremor source amplitudes for the northern Cascadia episodic tremor and slip (ETS) events from 2007-2010 and find they exhibit similar spatiotemporal patterns of radiated energy from tectonic tremor. In the initiation phase of each event, during which tremor starts downdip and moves updip over ~8 days, the tremor area and tremor amplitudes increase quasi-linearly, implying a constant radiated energy rate per unit area and a diffusional process for tremor migration. During this time, tremor amplitudes do not exhibit a strong sensitivity to tidal stress fluctuations. Once the tremor fills the downdip width of the tremoring region, the ETS events begin to propagate to the north and south at a constant rate, with the amplitudes being strongly modulated by tidal stresses. This implies a generally low effective normal stress or low effective friction along the plate interface, and that stress or friction begins higher during the

initiation of an ETS event and decreases as the ETS grows to the point where small tidal stress fluctuations can modulate the energy released during slow slip.

Using a 2-year deployment of 70 broadband seismometers, and several other seismic data sets, I invert local earthquake travel times to obtain 3-D *P*- and *S*-wave velocity models of the Mount St. Helens (MSH) region. Principal features of the 3-D models include: (1) Low *P*- and *S*-wave velocities along the St. Helens seismic Zone (SHZ), striking NNW-SSE north of MSH from near the surface to where we lose resolution at 15–20 km depth. This anomaly corresponds to high conductivity as imaged by magnetotelluric studies. The SHZ could represent a zone of crustal weakness with the presence of fluids, fractured rock, and/or sediments from the accretion of the Siletzia terrane; (2) A 4-5% negative *P*- and *S*-wave velocity anomaly beneath MSH at depths of 6-15 km with a quasi-cylindrical geometry and a diameter of 5 km, probably indicating a magma storage region. Based on resolution testing of similar-sized features, it is possible that this velocity anomaly is narrower and slower. Assuming approximately 1% partial melt per % velocity variation, this region could contain up to 5-10 km^3 of partial melt; (3) A broad, very low *P*-wave velocity region below 10-km depth extending between Mount Adams and Mount Rainier along and to the east of the main Cascade arc, which is likely due to high-temperature arc crust and the possible presence of melt; (4) Several anomalies associated with surface-mapped features, including high-velocity igneous units such as the Spud Mountain, Spirit Lake, McCoy Creek, Silver Star, and Tatoosh plutons and low velocities in the Chehalis sedimentary basin and the Indian Heaven volcanic field.

This dissertation includes two sets of supplementary files: (1) a set of 3-D *P*- and *S*-wave velocity models; and (2) a catalog of earthquakes relocated using 3-D velocity models.

Table of Contents

List of figures

List of tables

I. Introduction

In northern Cascadia, the Juan de Fuca plate subducts beneath North America at an oblique angle. It has the potential to generate large M9 thrust earthquakes in the seismogenic zone between depths of 5-30 km (Atwater, 1987). Downdip of the seismogenic zone, the plate interface experiences periodic slow-slip events and associated tectonic tremor (Rogers and Dragert, 2003), which transfer stress updip (Wech and Creager, 2011), building stress within the seismogenic zone until the next megathrust earthquake. Further downdip of the slow slip region, fluids released by the Juan de Fuca plate enable melting within the mantle wedge; these melts rise and form the Cascade volcanic arc. In this dissertation, I explore slow slip processes at the subduction interface and the magmatic systems beneath Cascades volcanoes, with the goal of contributing to theoretical models for subduction zones and volcanoes, and the seismicity which occurs at both.

Large episodic tremor and slip (ETS) events in northern Cascadia typically occur every 12-16 months (Rogers and Dragert, 2003; Brudzinski and Allen, 2007), and are associated with moment release equivalent to a moment magnitude 6.1-6.7 earthquake, as inferred from GPS measurements (Aguiar et al., 2009; Schmidt and Gao, 2010). Since tremor also occurs during this time, it is closely associated with slip on the plate interface. There is also a relationship between small stress fluctuations and the occurrence of tremor. Rubinstein et al. (2007) showed evidence for triggering of tremor under Vancouver Island during the passing of Love waves from the Mw=7.8 2002 Denali, Alaska earthquake. The shear stresses from these waves were on the order of 40 kPa on the plate interface. Rubinstein et al. (2008) and Ide (2010) presented further evidence for tremor being modulated by tidal stresses on the order of several kPa.

While there is a substantial literature regarding detection and location of tremor at several subduction zones, tremor amplitudes have received far less attention. The first systematic study of tremor amplitudes was in Japan by Maeda and Obara (2009). They showed that seismic energy radiation of tremor varies by about an order of magnitude in space and time, and that its temporal pattern is consistent with slow slip estimated from tilt records. Yabe and Ide (2014) calculated tremor amplitudes at several subduction zones around the world and classified tremoring regions based on the tremor zone width, the variability of tremor amplitudes, and the mode of tremor migration. Yabe et al. (2015) focused on tremor amplitudes in Japan and Cascadia, and how they varied spatially with regards to estimated tidal stresses along the plate interface.

In Chapter 2 of this dissertation I examine the northern Cascadia ETS events of 2007, 2008, 2009, and 2010. I analyze the tremor catalog produced by the Waveform Envelope Cross-Correlation (WECC) method (Wech and Creager, 2008; Wech, 2010) and determine amplitudes for each 5-minute window of tremor using data from the CAFE and Array of Arrays experiments. I find that each ETS event initiates with a quasi-linear growth in tremor amplitude and tremor area over the first 5-8 days. This is followed by a longer propagation phase, during which the tremor amplitude fluctuates wildly, synchronized with tidal forces, as the tremor follows the ETS rupture front along the strike of the plate interface. This pattern implies a generally low effective normal stress or low effective friction along the plate interface, which begins higher during the initiation of an ETS event and decreases as the ETS grows, reaching a point where small tidal stress fluctuations can modulate the tremor energy released during slow slip.

The main Cascade Range volcanic arc stretches from northern California to southern British Columbia. In southern Washington and northern Oregon the arc consists of Mounts Hood and Adams, as well as former volcanic center Goat Rocks and a number of Quaternary-aged volcanic vents. These centers are primarily basaltic to andesitic in composition (Hildreth, 2007). There is also diffuse Quaternary-aged volcanism stretching eastwards (Simcoe) and westwards (Indian Heaven, Boring). This part of the arc also has two volcanoes located trenchward of the main volcanic axis: Mount Rainier, located ~35 km west of the arc; and Mount St. Helens (MSH), the most active Cascade volcano of the past 2000 years, located almost 50 km towards the trench from Mount Adams (Hildreth, 2007).

MSH lies along the trend of the St. Helens seismic zone (SHZ), which shows a ~100-km-long pattern of WNW-trending seismicity at depths shallower than ~16 km (Weaver and Smith, 1983; Weaver et al., 1987). A similar-trending seismic zone is present near Mount Rainier, known as the Western Rainier seismic zone (WRSZ). Most of the earthquakes in the SHZ and WRSZ show evidence of right-lateral strike slip motion (Weaver et al., 1987; Moran et al., 1999). The SHZ is thought to accommodate north-south crustal shortening in the region caused by the clockwise rotation of the Oregon crustal block, which is related to nortwestwards movement of the Pacific plate (Wells et al., 1998; Wells and Simpson, 2001; Brocher et al., 2017). The SHZ could possibly represent a localized tectonic boundary related to the accretion of the Siletzia terrane at ~50 Ma (Snavely et al., 1968; Duncan, 1982; Wells et al., 2014). If so, it could be a major zone of weakness throughout much of the crust that, among other things, could allow magma to ascend and erupt trenchwards of the Cascade volcanic axis at volcanoes like MSH and Mount Rainier (Weaver et al., 1987).

To improve our understanding of the geology and current magmatic setting of MSH, in Chapter 3 I present results from a local earthquake tomography study. I obtained a high-resolution 3-D *P*- and *S*-wave model from 0-20 km depth in a 50-km radius area around MSH, using data collected by the imaging Magma Under St. Helens (iMUSH) experiment. This is the highest-resolution 3-D *P*-wave velocity model yet determined for the MSH area, and is the first-ever high-resolution *S*-wave velocity model.

II. Initiation and propagation phases of northern Cascadia ETS

2.1. Introduction

Large episodic tremor and slip (ETS) events in northern Cascadia typically occur every 12-16 months (Rogers and Dragert, 2003; Brudzinski and Allen, 2007), with smaller tremor events occurring in the months between. Major ETS events follow a general pattern, beginning with scattered tremor in the downdip portion of the plate interface at depths of 40-45 km. The tremor then begins to move updip over several days (Wech and Creager, 2011) before migrating along strike at rates of 7-12 km a day (Houston et al., 2011).

Large ETS events in Cascadia typically are associated with moment release equivalent to a moment magnitude 6.1-6.7 earthquake, as inferred from GPS measurements (Aguiar et al., 2009; Schmidt and Gao, 2010). Since tremor occurs simultaneously with the GPS-measured movements, tremor occurrence is likely closely associated with slip on the plate interface. There is also a relationship between small stress fluctuations and the occurrence of tremor. Rubinstein et al. (2007) showed evidence for triggering of tremor under Vancouver Island during the passing of Love waves from the Mw=7.8 2002 Denali, Alaska earthquake. The shear stresses from these waves were on the order of 40 kPa on the plate interface. Rubinstein et al. (2008) and Ide (2010) presented additional instances of tremor being modulated by tidal stresses, which were on the order of several kPa.

While there is a substantial literature regarding detection and location of tremor at several subduction zones, tremor amplitudes have received far less attention. Maeda and Obara (2009) performed the first systematic study of tremor amplitudes in Japan. They showed that seismic energy radiation of tremor varies by about an order of magnitude in space and time, and that its temporal pattern is consistent with slow slip estimated from tilt records. Yabe and Ide (2014)

calculated tremor amplitudes at several subduction zones around the world and classified tremoring regions based on the tremor zone width, the variability of tremor amplitudes, and the mode of tremor migration. Finally, Yabe et al. (2015) analyzed how tremor amplitudes in Japan and Cascadia varied spatially with respect to estimated tidal stresses along the plate interface.

The northern Cascadia ETS events of 2007, 2008, 2009, and 2010 are the focus of this study. In this paper we analyze the tremor catalog produced by the Waveform Envelope Cross-Correlation (WECC) method (Wech and Creager, 2008; Wech 2010) and determine amplitudes for each 5-minute window of tremor, using data from the CAFE and Array of Arrays experiments (Abers et al., 2009; Ghosh et al., 2012). We find that each ETS event initiates with a quasi-linear growth in tremor amplitude and tremor area over the first 5-8 days, followed by a longer propagation phase during which the tremor amplitude fluctuates wildly in conjunction with tidal forces as tremor sources migrate along strike in parallel with the ETS rupture front.

2.2. Data

We use continuous three-component short-period and broadband velocity seismograms from the Transportable Array (TA), Cascadia Array For Earthscope (CAFE), and Array of Arrays experiments, spanning 2006-2011 (Figure 1). The CAFE experiment ran from 2006 to 2008, with several instruments remaining through 2011, while the Array of Arrays lasted from 2009 to 2011. Data from a total of 9 arrays and 13 single stations are used.

2.3. Tremor source amplitudes

In this study tremor locations were determined using a waveform envelope cross-correlation method (Wech and Creager, 2008). For each vertical-component station seismogram,

we demeaned, tapered, deconvolved the instrument response to velocity, bandpass filtered the seismogram at 1.5 to 5 Hz, then calculated the envelope of the data before applying antialiasing filters and resampling to 1 sample per second. We took the median at each time-step of all stations in each array of the Array of Arrays in order to increase the signal-to-noise ratio, creating one time series per array. Each of these array stacks contains between 9-20 stations at an array aperture of less than 1 km. For all isolated stations and array stacks, we combined the power of the three components and obtained the average surface velocity amplitude for all 50% overlapping 5-minute windows in the study period.

For each 5-minute window with a tremor location, we corrected each available station amplitude for geometric spreading and attenuation, as follows:

$$A_{corr} = A_{obs} R \exp\left[\frac{\pi f_c \mathrm{R}}{Q V_s}\right], \quad (1)$$

where A_{obs} is the root-mean square (rms) velocity (m/s) at the station for that 5-minute window, R is the straight-line source-receiver distance, f_c is the center frequency of 2 Hz, Q is the quality factor for shear waves of 180, and V_s is the shear-wave velocity of 3.5 km/s. We have tried different values of Q ranging from 50 to 2000 and find that this affects the mean tremor amplitudes but has little effect on relative amplitudes (see Supplementary Materials). The values used in this study compare favorable to analyses by Baltay and Beroza (2013) and Yabe et al. (2014), which used tremor data to examine seismic wave attenuation.

We then performed a least-squares inversion of the log of corrected (eq. 1) station amplitude to determine the log of tremor source amplitude and for station corrections (as in Maeda and Obara, 2009). The amplitudes presented here are in the form of relative mean radiated energy rate integrated over the associated time intervals.

$$\frac{1}{2}\log\left(\dot{W}^J\right) + \log\left(A_s^i\right) = \log\left(A_{corr}^{ij}\right), \quad (2)$$

where $\dot{W}^J$ is proportional to the radiated energy rate for the *j*th tremor source and A_s^i is a dimensionless station correction accounting for the geology near the *i*th station (see Table S1). We form a model vector, *m*, that contains $\frac{1}{2}\log\left(\dot{W}^J\right)$ and $\log\left(A_s^i\right)$, and a data vector, *d*, that contains $\log\left(A_{corr}^{ij}\right)$. They are connected through a matrix *G* containing ones and zeros,

$$Gm = d. \quad (3)$$

An additional equation specifies that $\sum_{i=1}^{N} A_s^i = 0$. This system is solved for *m* using least squares.

2.4. Results

In all four ETS events that we examined, the initial tremor locations began downdip, near the 45-km depth contour of the plate interface (Figures 2-5, part a). The area in which tremor occurred increased quasi-linearly as the tremor locations moved updip over several days, at which point they began propagating along strike to the north and south. We calculated area contours of tremor by first calculating the number of tremor epicenters per square km smoothed with a 3-km half-width Gaussian operator, then contouring the data to find the area containing 75% of tremor within a given time period. The quasi-linear increase in the area experiencing tremor is evident regardless of the time-averaging window used, although it is not as clear for time periods less than two hours.

The temporal variations in tremor amplitudes and locations along strike are similar for each of the ETS events we studied (Figures 2-5, part b). Each ETS event began with lower amplitudes that increased quasi-linearly during the first 5-8 days (Figures 2-5, part c, Figure 6a).

Once the tremor began to propagate along strike to the north and south, the amplitudes began to vary by over an order of magnitude. These strong fluctuations contrast with typical source-time functions of regular earthquakes, which are too brief to experience tidal modulation during their ruptures. It is also possible to see rapid tremor reversals (RTRs) in the time-distance plots, since RTRs generally have the highest amplitudes (Thomas et al., 2013), and propagate at velocities of 7-17 km/h in a direction opposite to the overall ETS movement (Houston et al., 2011).

Tremor source amplitudes during ETS events peaked between 15 to 30 km downdip (Figure 8) of the updip tremor limit calculated by Wech and Creager (2011). This is also the region where most ETS tremor occurs, whereas shorter inter-ETS tremor episodes generally occur further downdip and have lower amplitudes by 30-50%. Similar behavior has been observed with low-frequency earthquake (LFE) magnitudes decreasing with greater depths beneath northern Washington (Sweet thesis, 2014) and Vancouver Island (Bostock et al., 2015). LFE magnitudes have also been shown to be lower between ETS events than during them (Chestler and Creager, 2017).

Examination of the power spectrum of the tremor amplitudes during the ETS initiation phase reveals a broad peak at around 24 hours and another broad peak at around 12 hours. However, the amplitude power spectrum during the propagation phase of ETS events reveals much clearer peaks at periods of 12.0 and 12.4 hours, as well as 23.9 and 25.8 hours (Figure 7). These are the primary tidal periods and have been found previously to have a strong periodic signal in borehole strainmeters in Cascadia during slow slip events (Hawthorne and Rubin, 2010), as well as in LFE occurrence in Japan (Aso et al., 2013). In addition to the 4 ETS events presented above, we also examined the 11 largest inter-ETS events, which lasted from 4-10 days

and contained 20-80 hours of tremor. None of the inter-ETS events exhibited clear spectral peaks at these tidal periods.

2.5. Discussion

In recent studies (e.g. Houston, 2015) an explanation for tremor amplitude modulation by tides has been proposed that invokes a plate interface that is more sensitive to small stresses after it has been ruptured during the initial passage of the rupture front. This would indicate low effective normal stress or low effective friction where tidal modulation occurs. In our results, tidal modulation appears weaker during the initiation phase. This is analogous on a broad scale to temporal amplitude variations reported by Houston (2015) based on a smaller-scale ETS study. As in Houston (2015), we infer from the tidal insensitivity during the early part of the ETS that the stress state during the initiation phase is higher than that during tidal stress fluctuations (e.g., Figure 5 of Houston 2015).

There are no clear tremor amplitude spectral peaks at the four largest tidal periods during large (4-10 days-long) inter-ETS tremor episodes we have examined. This could be because the signal is too short or noisy to interpret reasonably, or because the smaller events involve less slip than the larger ones so that the plate interface is never reduced to a sufficiently weak stress state. Alternatively, it may be that these events remain in the initiation phase and never develop into the along-strike propagation phase.

The change in the number of tremors as well as their amplitudes with downdip distance may indicate varying properties of the plate interface. Regardless of the actual mechanism behind tremor and slip, it appears that the ideal conditions for its occurrence are within 15-30 km of the updip tremor limit beneath northern Washington. Further updip or downdip of this region,

fewer and smaller tremors occur, indicating that there is not an abrupt change in plate interface properties, but rather a gradual change. Similarly, the number and amplitudes of tremors vary along strike, as has been observed previously in Cascadia, Japan, and other locations (Yabe and Ide, 2014). These characteristics reflect the heterogeneity of the plate interface, which can be described by different mechanical models, including the the strong or weak tremor patches of Ghosh et al. (2012) and Yabe and Ide (2014), or the brittle and ductile deforming regions of Chestler and Creager (2017).

We find a linear or quasi-linear increase in tremoring area and source amplitude over the first 5-8 days of the northern Cascadia ETS events (Figure 6). This implies a constant radiated energy rate per unit area of the plate interface during the initiation of ETS events. The linear increase in tremor area could be related to spatial diffusion of stress in the two-dimensional fault plane (Figure 10). By fitting a straight line through the total area experiencing tremor during the initiation phases of the 4 ETS events (Figure 9), we obtain slopes of 1.3-4.4 * 10^3 m^2/s, similar to diffusional coefficients of 10^4 m^2/s found by Ide (2010) in Japan and Houston et al. (2011) in Cascadia. Though this has been measured in a different way, like the studies of Ide and Houston et al it suggests a diffusion process is responsible for tremor movement during the ETS initiation with distance moved proportional to the square root of time. The factor of 2 to 5 difference between our result and previous work may be related to measurement uncertainty and different methods of measurement.

In contrast to the initiation phase, the subsequent propagation phase is not dominated by diffusion (Figure 10). During this time the tremoring region is bounded at the updip and downdip edges and the tremor front propagates at a relatively constant velocity between 7-12 km/day (Houston et al., 2011). During this time, the propagation rate along strike may be controlled

more by the dip-parallel width of the tremoring zone and the static stress buildup from already-slipped regions behind the slow slip front (Shibazaki et al., 2012).

2.6. Conclusion

The northern Cascadia ETS events from 2007-2010 exhibited similar spatiotemporal patterns of radiated energy from tectonic tremor. In the initiation phase of each event, during which tremor started downdip and moved updip over ~8 days, the tremor area and tremor amplitudes increased quasi-linearly, implying a constant radiated energy rate per unit area and a diffusional process for tremor spread. During this time, the tremor amplitudes did not exhibit a strong sensitivity to tidal stress fluctuations. Once the tremor filled the downdip width of the tremoring region, the ETS events began to propagate to the north and south at a constant rate, with the amplitudes being strongly modulated by tidal stresses. This implies a generally low effective normal stress or low effective friction along the plate interface. Our amplitude observations suggest that stress states are initially higher during the initiation of an ETS event and decrease as the ETS grows, to the point where small tidal stress fluctuations can modulate the energy released during slow slip.

2.7. Supplementary material

We test the robustness of the amplitude inversion by examining the $\log_{10}$ amplitude misfit for each station/array as a function of hypocentral distance (Figure S1). The misfit exhibits a surprisingly log-normal distribution without significantly heavy tails, although there is some increase with distance. This is surprising because we do not remove noisy data that could potentially bias source amplitudes to higher values. Furthermore, the statistics (mean and

standard deviation) do not vary much with hypocentral distance. This is largely because we have chosen to use only very quiet three-component single stations and arrays that are significant distances from cultural noise. Figure S1 also indicates that our very crude correction for geometric spreading (dividing by hypocentral distance) is sufficient for our purposes.

We tested multiple values of Q in our tremor amplitude inversion (Figure S2). When plotting the residual of the predicted station/array amplitude for each tremor versus hypocentral distance, we see an increase in residual with distance, especially for lower values of Q. As Q grows, the residual-with-distance trend approaches horizontal. The increase with distance is likely due to noise being introduced to the inversion from stations that are too far from the tremor source to exhibit a tremor signal.

Table S1 shows the station/array correction values for each year of the analysis. The product of each column equals 1. Station correction values are generally consistent year-to-year.

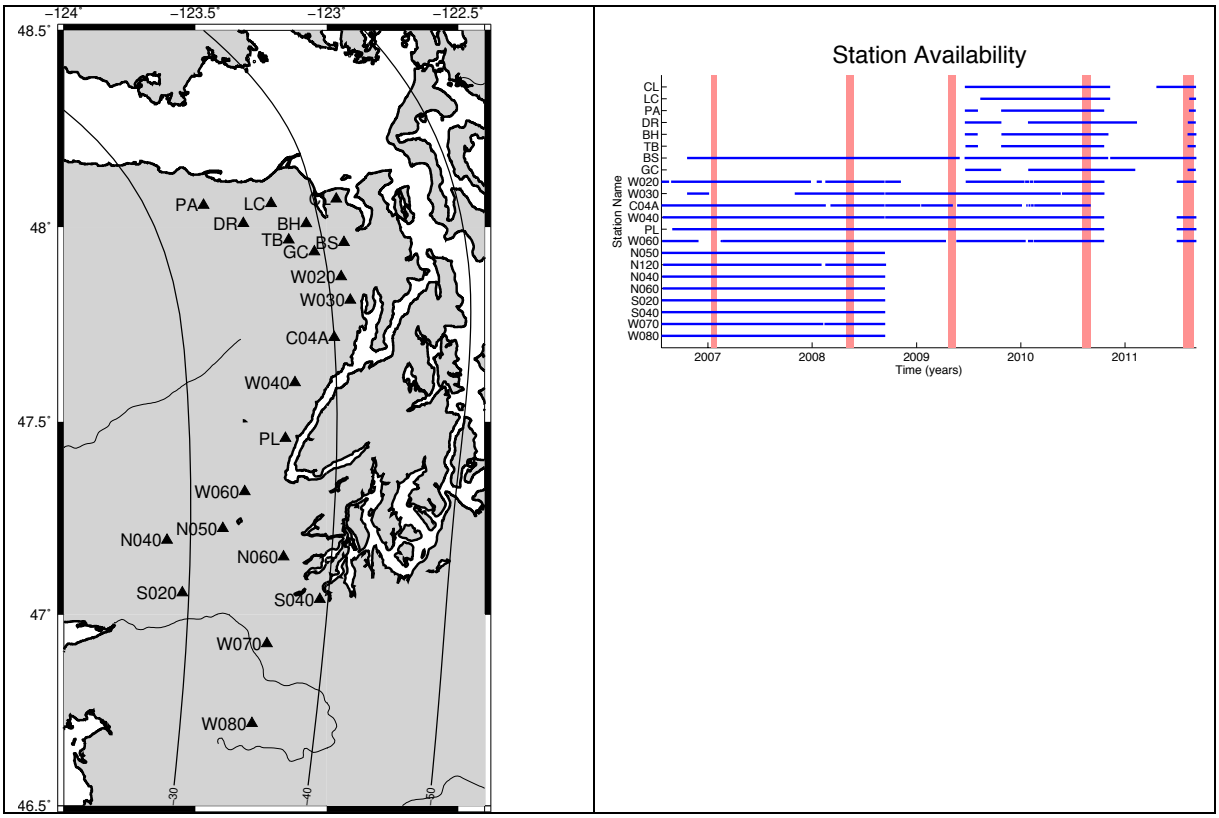

Figure 2.1. Station and array geometry and timing.
Left: Station (4-letter codes) and array (2-letter codes) locations used in the analysis. Black lines show depth to plate interface from McCrory et al., 2012. Right: Data availability for stations and arrays. Pink bars indicate ETS time periods.

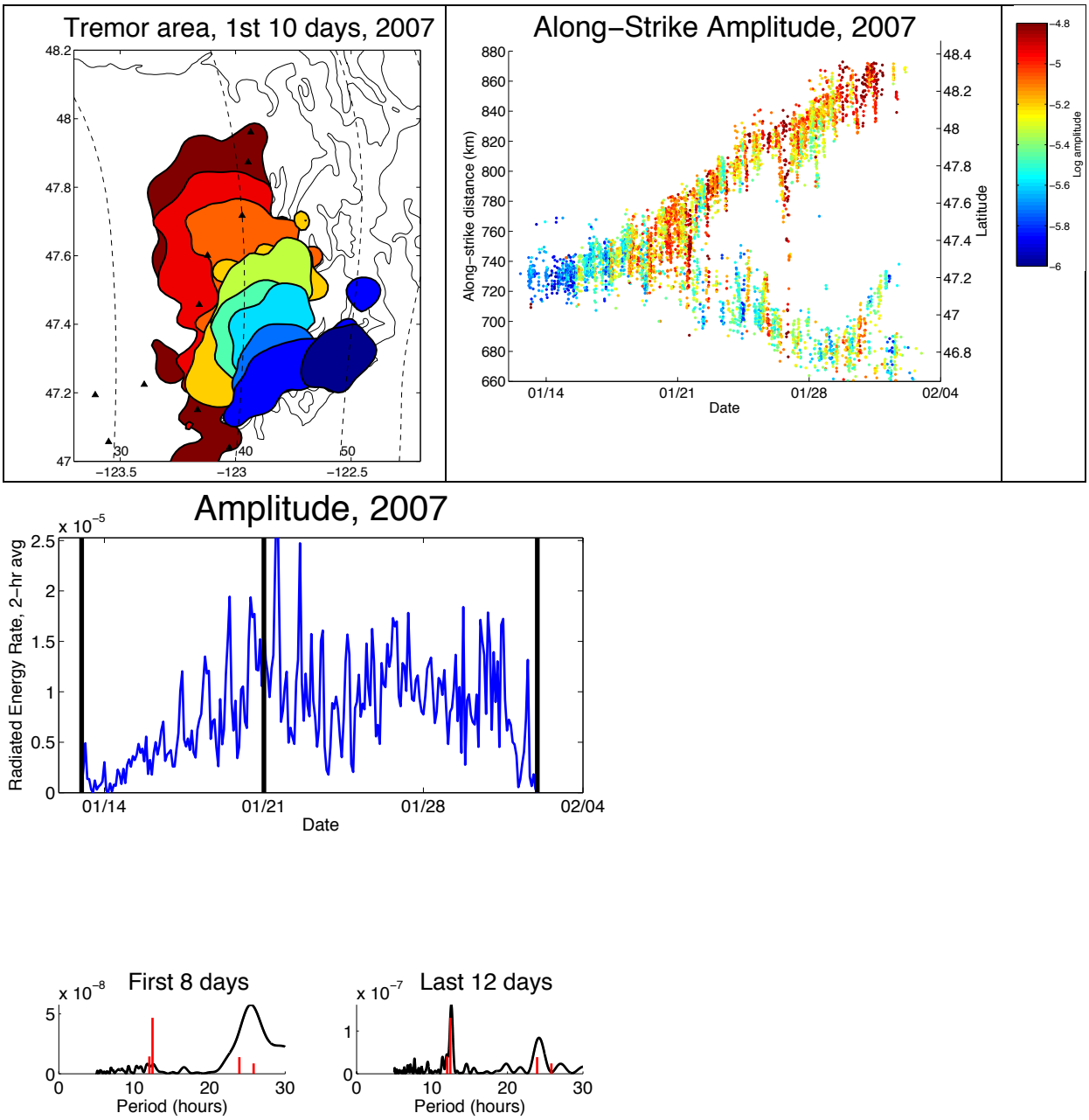

Figure 2.2. Tremor area, amplitudes, and tidal modulation for 2007 ETS event.
Top left. Contours of tremor area for the first 10 days of the 2007 ETS events, obtained by calculating the tremor epicenters per square km, then contouring the data to find the area containing 75% of tremor. **Top right**. Tremor source amplitudes as they vary along strike and through time. **Middle**. 2-hr average tremor amplitude during the 2007 ETS event. **Bottom**. Power spectra of tremor source amplitudes for the first 8 days and the last 12 days of the 2007 ETS event.

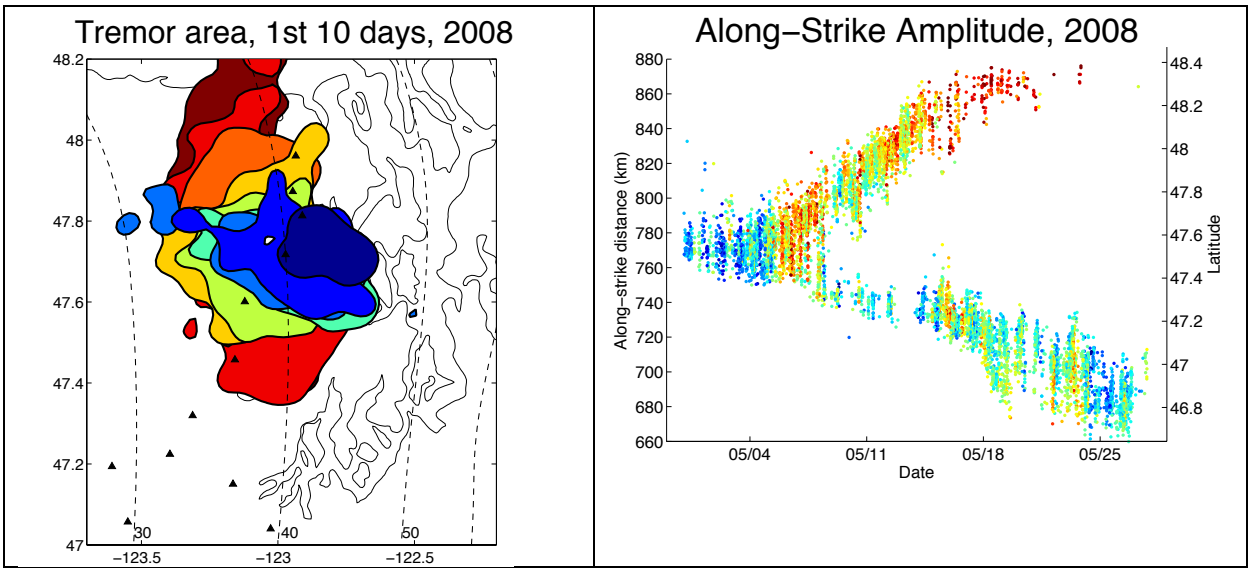

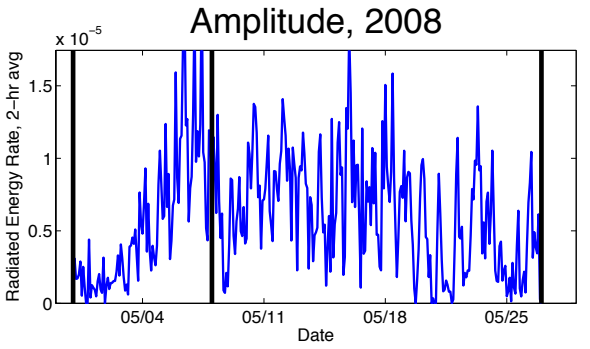

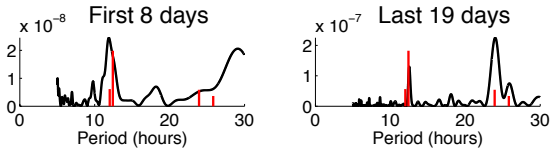

Figure 2.3. Tremor area, amplitudes, and tidal modulation for 2008 ETS event.

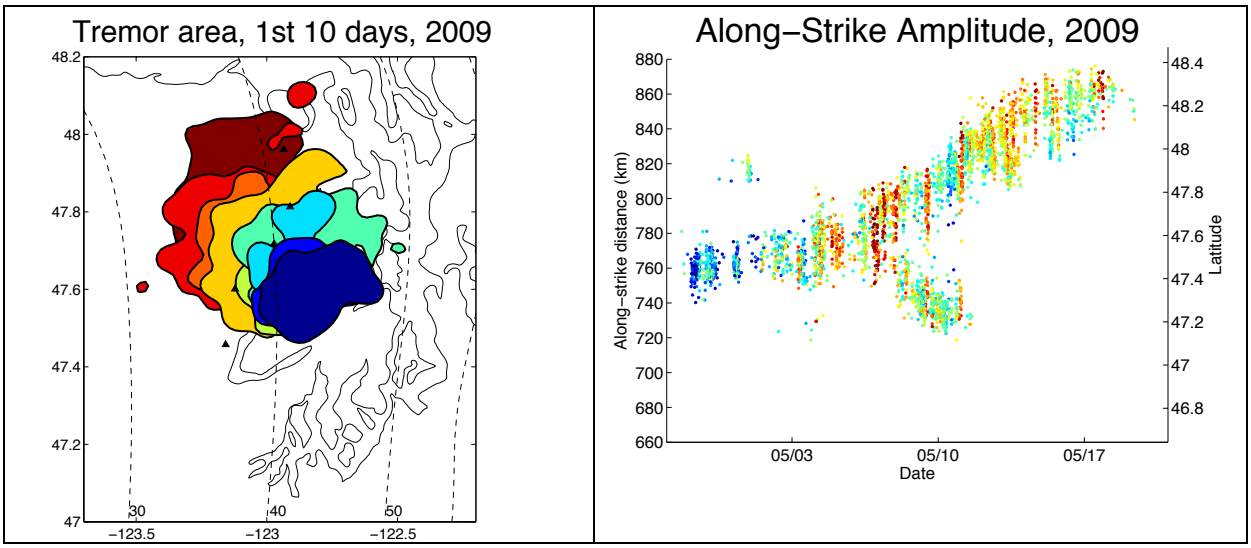

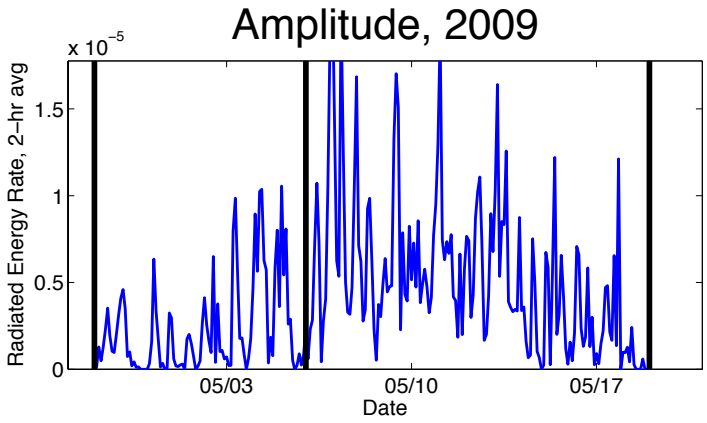

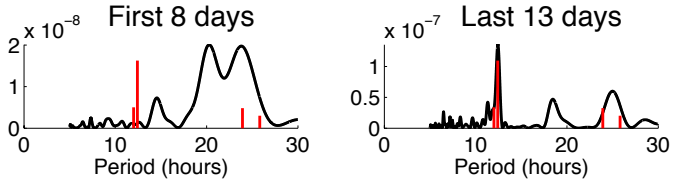

Figure 2.4. Tremor area, amplitudes, and tidal modulation for 2009 ETS event.

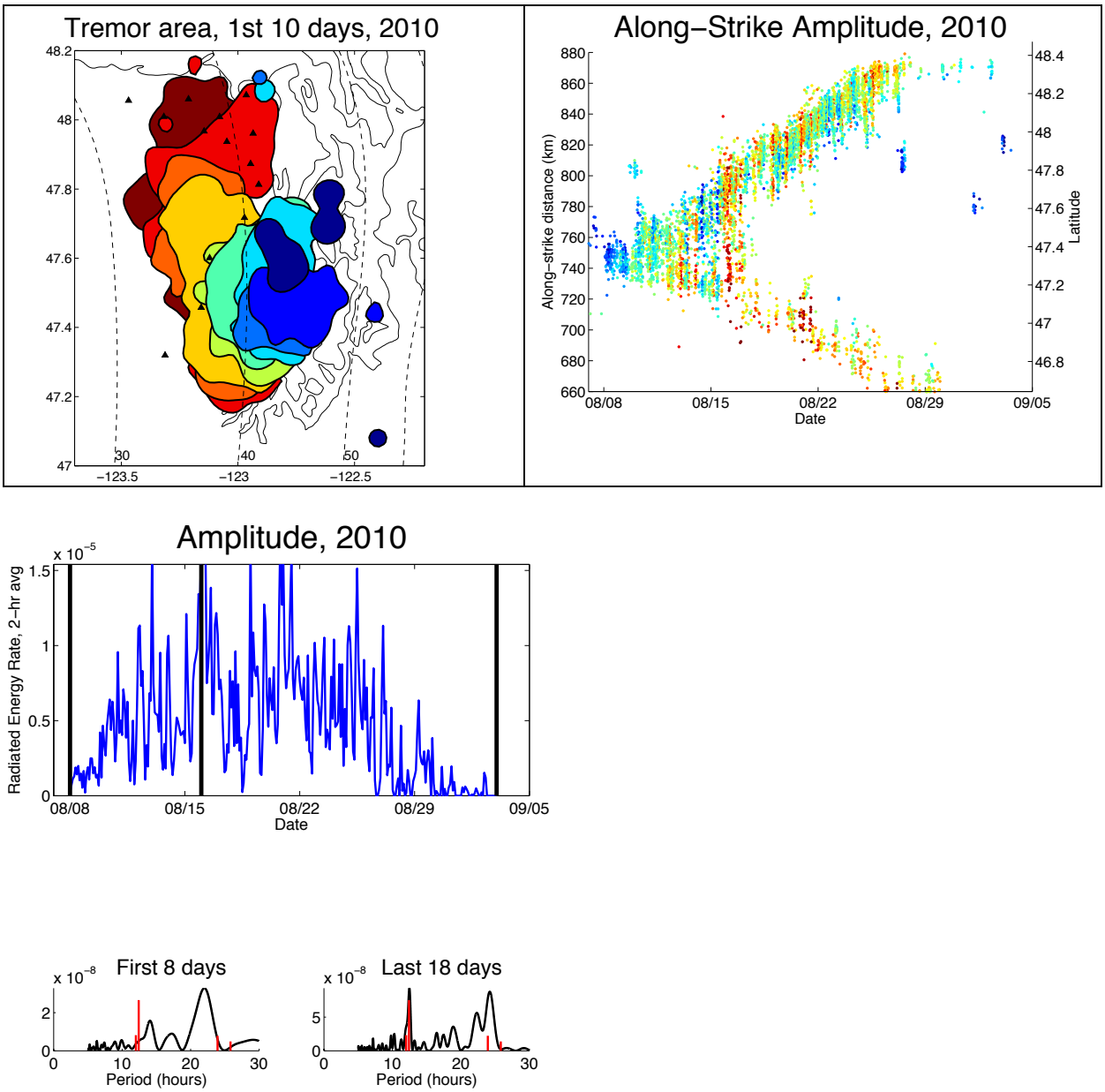

Figure 2.5. Tremor area, amplitudes, and tidal modulation for 2010 ETS event.

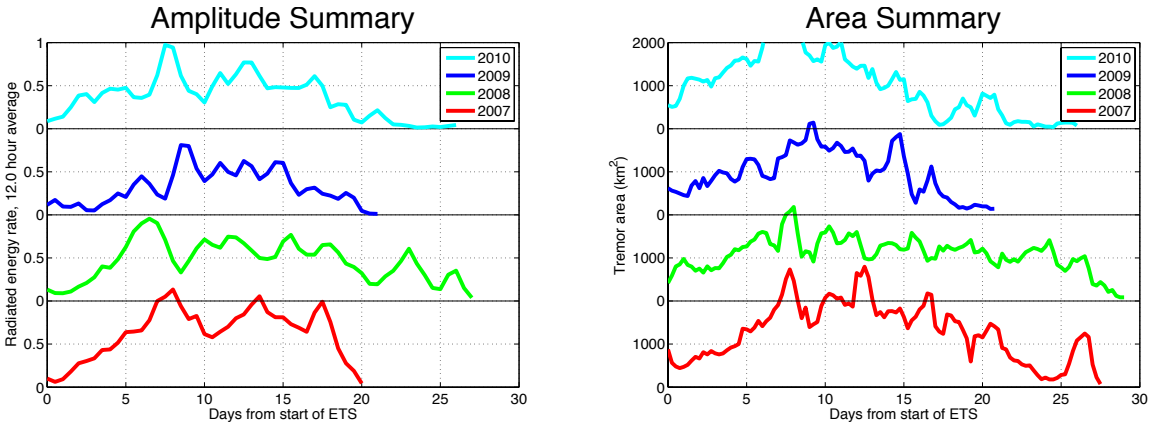

Figure 2.6. Summary of tremor amplitude and area.

Summary of tremor source amplitude and tremoring area for the 2007-2010 ETS events, with quasi-linear increase over the first ~8 days, followed by fluctuation.

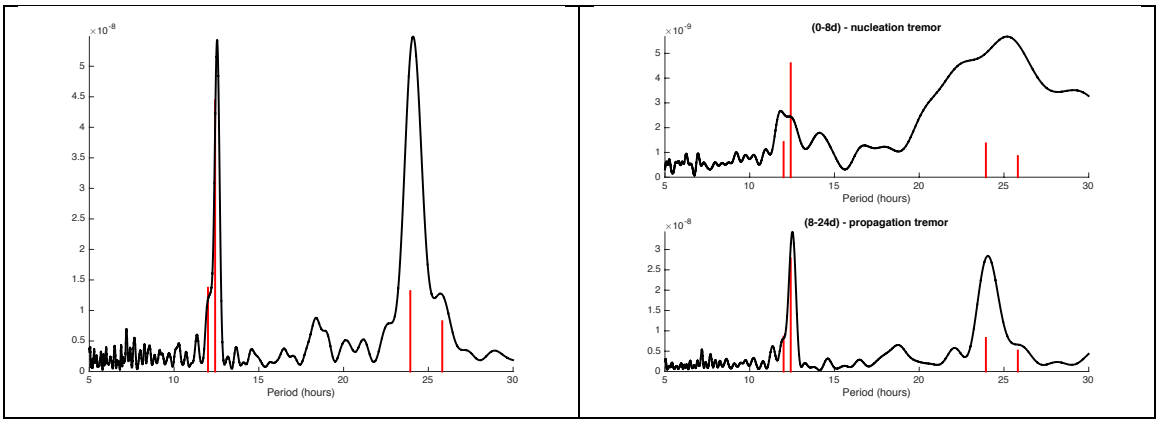

Figure 2.7. Tremor amplitude spectra.

Amplitude spectra over all ETS events (left), during ETS initiation (top right), and during ETS propagation (bottom right), with sharp peaks at the primary tidal periods (red lines, scaled with relative strength).

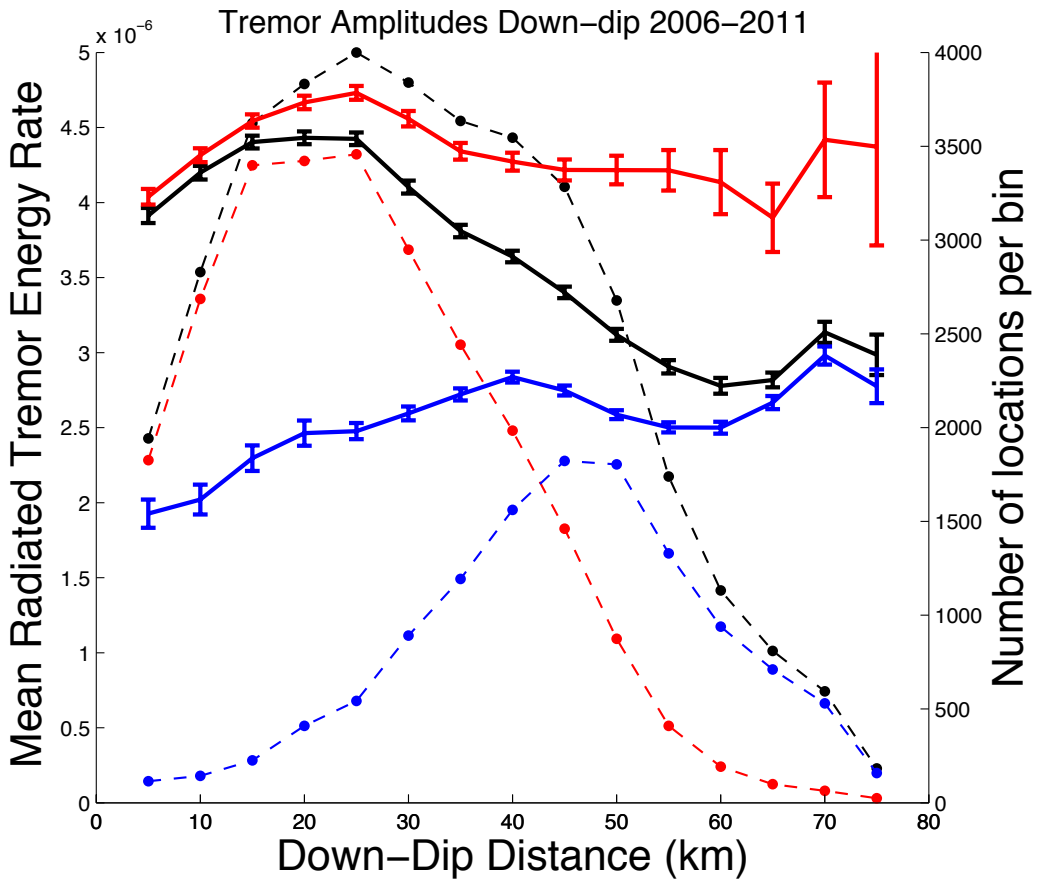

Figure 2.8. Average source amplitudes downdip.

Amplitudes for each 5-km bin downdip of the updip tremor limit (solid line with error bars) and total number of locations (dashed line) are plotted for **ETS events** (red), **inter-ETS events** (blue), and **all tremor events** (black) for the study period.

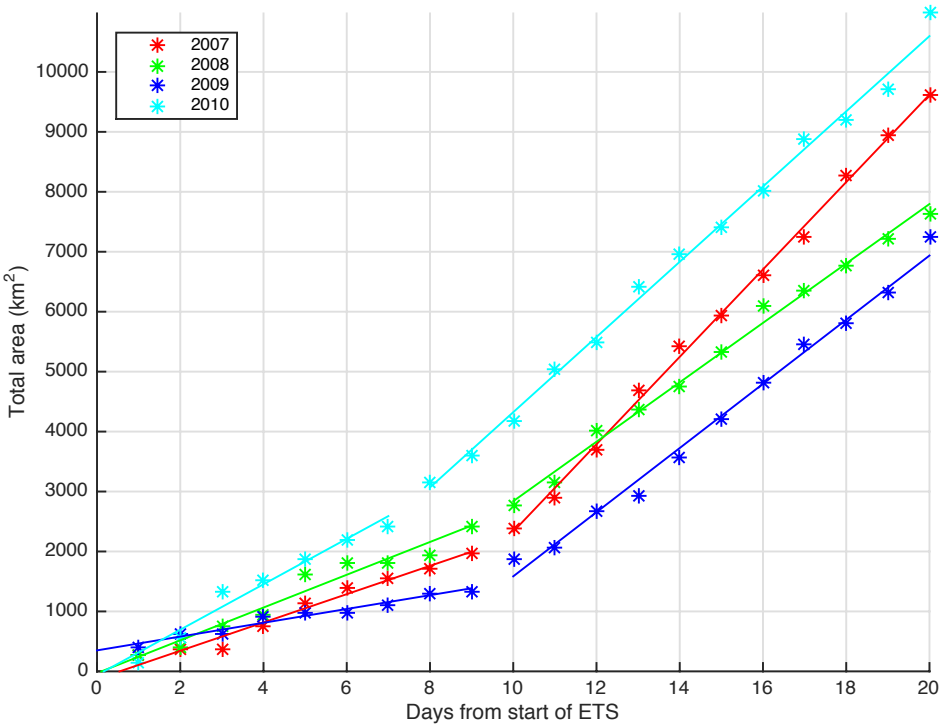

Figure 2.9. Total area vs. time.

Total area that underwent tremor vs. time for each ETS event. The slope of the lines for the first 7-9 days gives the diffusion coefficient during ETS initiation.

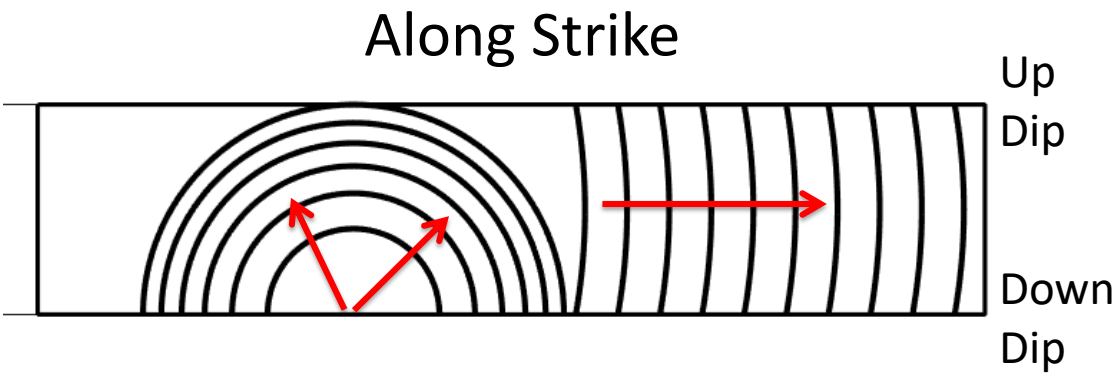

Figure 2.10. Conceptual tremor model.

Tremor initiation and propagation, showing diffusional growth during initiation (area proportional to time), and constant velocity during propagation.

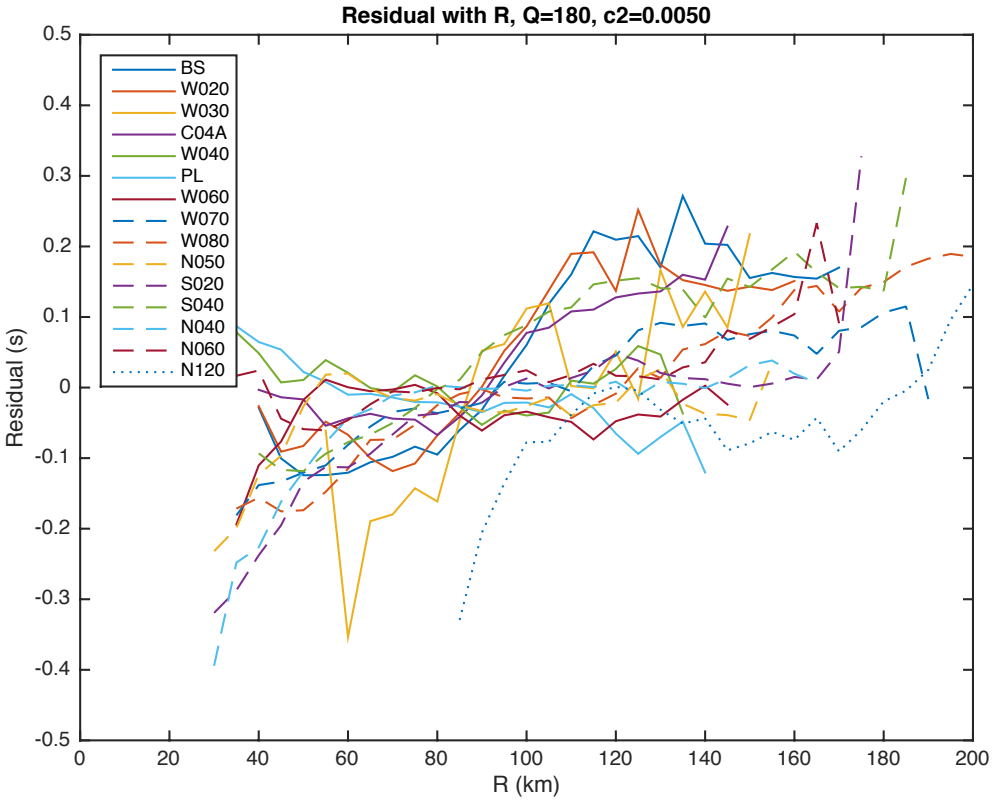

Figure 2.S1. All station amplitude residuals.

Individual mean station amplitude residuals with hypocentral distance, for Q=180, for all of 2007.

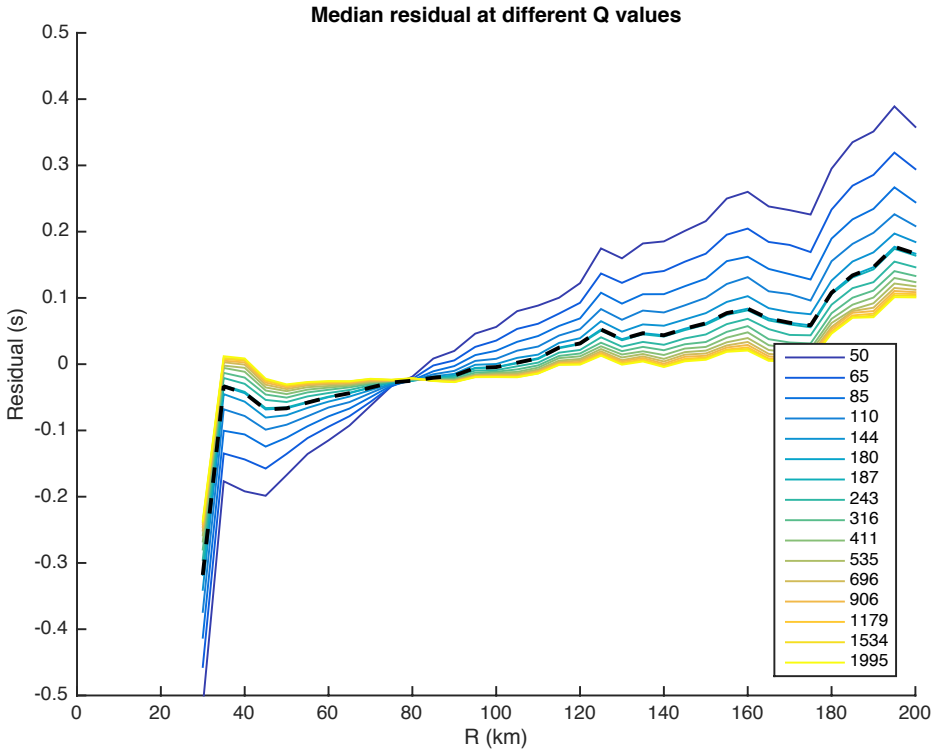

Figure 2.S2. Median station residual vs. Q.

Median residual for all station amplitudes in 2007 with hypocentral distance from the tremor source, for different values of the attenuation parameter, Q. The value used in the final analysis is 180, shown in the black, dotted line.

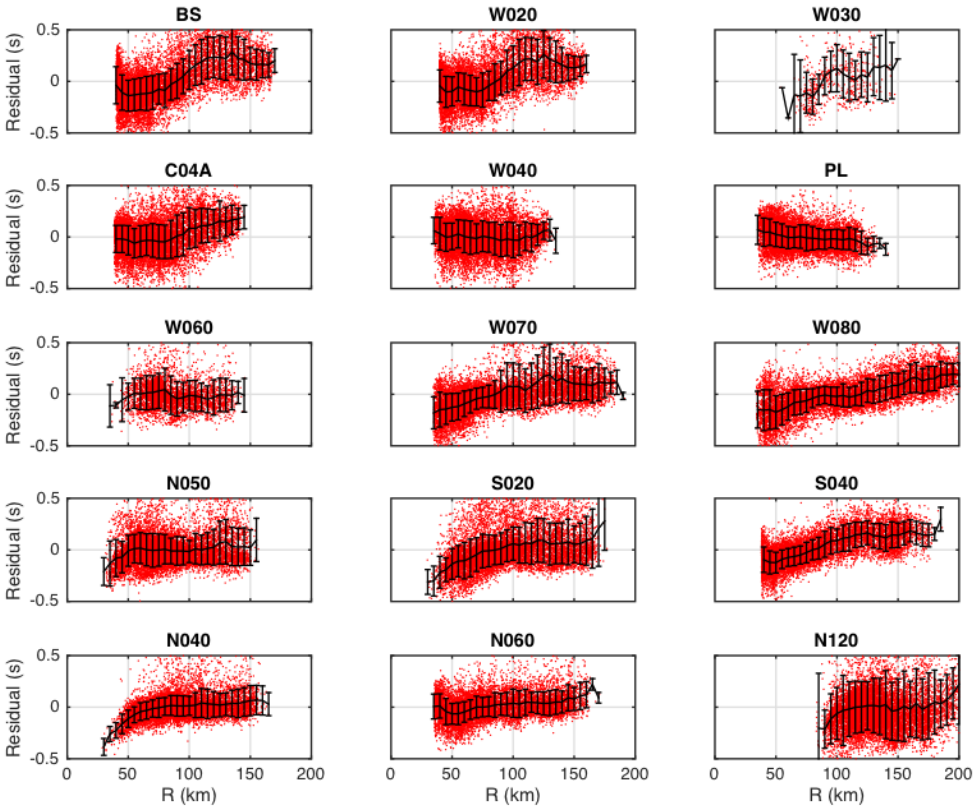

Figure 2.S3. Individual station amplitude residual.

Station amplitude residual (red dots) and mean and standard deviation of residual (black lines) for all tremor during 2007.

	Initiation	Propagation
Duration	~8 days	2-3 weeks
Direction	Up dip	Along strike
Total Tremor Area	$A \propto \tau$: 150-400 km^2/day	$A \propto \tau$: 500-750 km^2/day
Bounded?	No: $L \propto A^{1/2} \propto \tau^{1/2}$ Diffusion	Yes: $L = A/W \propto \tau$ (W=50km)
Amplitude	$\propto \tau$	No long term trend
Area per day	$\propto \tau$ so Amp $\propto$ Area	
Tidal Sensitivity	Weak	Very strong
Propagation Speed	Changes	7-12 km/day

Table 2.1. Summary of tremor amplitude results.

Station	Year			
	2007	2008	2009	2010
BH			0.63	0.62
BS	0.88	0.78	0.8	0.8
CL			5.06	3.1
DR			0.85	0.79
GC			0.89	1
LC			1.25	1.07
PA			1.01	0.94
PL	0.66	0.69	0.82	0.97
TB			0.89	1
C04A	2.7	2.87	2.74	3.06
N040	1.08	1.2		
N050	1.17	1.01		
N060	0.5	0.48		
N120	4.39	7.05		
S020	2.04	1.9		
S040	0.74	0.7		
W020	0.35	0.33	0.37	0.41
W030	0.76	0.67	0.72	0.77
W040	0.42	0.45	0.48	0.51
W060	1.19	1.28	1.58	1.71
W070	1.07	0.94		
W080	1.09	1.01		

Table 2.S1. Station correction values.

III. Local earthquake *Vp* and *Vs* tomography in the Mount St Helens region with the iMUSH broadband array

3.1. Introduction

The southwest Washington Cascades have a complicated tectonic history, which affects the current distribution of earthquakes, volcanoes, mineral deposits, and human settlement. At around 56-49 Ma, the basaltic Siletz terrane was erupted and subsequently accreted onto the westward edge of the North American continent (Snavely et al., 1968; Duncan, 1982; Wells et al., 2014). Outcrops of this terrane appear under different names in the modern forearc from Oregon to Vancouver Island, and active source seismic studies have shown the thickness to vary along strike from several km to 25 to 35 km (Trehu et al., 1994; Parsons et al., 1998). Associated with the accretion of Siletz is a series of marine and non-marine sedimentary rocks added to the edge of North America as part of the subduction complex, which have been interpreted as the cause of a highly conductive region of the crust (termed the southwest Washington Cascades Conductor, or SWCC) between Mounts St. Helens (MSH), Adams and Rainier (Stanley et al., 1987; Egbert and Booker, 1993). This conductive region has also been interpreted as an extensive region of mid-crustal partial melt connecting the three volcanoes (Hill et al., 2009).

Because of the complicated accretion history in the area, it is difficult to locate the eastern boundary of the Siletz terrane throughout Cascadia, even though a variety of methods have been used to constrain it. Using magnetic and pseudogravity data, Wells et al. (1998) placed the upper crustal boundary several tens of kilometers to the west of MSH. The terrane boundary has also been placed at MSH or along the St. Helens seismic zone (SHZ), based on active source tomography (Parsons et al., 1998) and geology- and GPS-derived block boundaries (McCaffrey et al., 2007; McCaffrey et al., 2013; Savage and Wells, 2015). Finally, recent studies using

USArray seismic data have placed the boundary, or at least some amount of subducted and underplated Siletz terrane, to the east of the Cascade Range, using teleseismic (Schmandt and Humphreys, 2011) or ambient noise (Gao et al., 2011) tomography.

Beginning in the late Oligocene and lasting several million years, the southern Washington Cascade magmatic arc experienced an increase in volcanic activity, with a series of mafic to silicic subaerial flows and plutonic bodies (Evarts et al., 1987). The largest of the currently exposed plutonic bodies include the Silver Star, Spirit Lake, and Tatoosh plutons (Evarts et al., 1987), and the Snoqualmie batholith, which is a little more recent (17-16 Ma, Chitwood, 1976), which stretch in a NNE line from near the Oregon-Washington border to the center of the Cascades in central Washington. These plutonic rocks are predominantly granitic to granodioritic, and were emplaced in the epizone, within ~5 km of the surface (Evarts et al., 1987). Subsequent volcanism in the MSH area was localized and relatively small in volume compared to the activity from 25-20 Ma (Evarts et al., 1987). Volcanic activity at MSH itself began about 300 ka, although it was not until 28 ka that eruptive activity increased significantly, and the edifice of MSH was largely constructed in the past 4000 years (Hoblitt et al., 1980; Mullineaux and Crandell, 1981; Clynne et al., 2005).

Currently, the main Cascade arc stretches from northern California to British Columbia. Near southern Washington, this consists of the stratovolcanoes Mounts Hood and Adams, as well as former volcanic center Goat Rocks and a number of Quaternary-aged volcanic vents, which are primarily basaltic to andesitic in composition (Hildreth, 2007). There is also diffuse Quaternary-aged volcanism (Hildreth, 2007) stretching eastwards (Simcoe) and westwards (Indian Heaven, Boring), and two volcanoes located trenchward of the main volcanic axis:

Mount Rainier, located ~35 km west of the arc, and MSH, the most active Cascades volcano of the past 2000 years, located almost 50 km towards the trench from Mount Adams (Figure 1b).

Mount St. Helens lies along the trend of the St. Helens seismic zone (SHZ), which shows a ~100-km long pattern of WNW-trending seismicity at depths shallower than ~16 km (Weaver and Smith, 1983; Weaver et al., 1987). A similar trending seismic zone is present near Mount Rainier, known as the Western Rainier seismic zone (WRSZ). Most of the earthquakes in the SHZ and WRSZ show evidence of right-lateral strike slip motion (Weaver et al., 1987; Moran et al., 1999). The SHZ is oriented in a way to accommodate the north-south crustal shortening in the region caused by the clockwise rotation of the Oregon crustal block, related to the movement of the Pacific plate towards the northwest (Wells et al., 1998; Wells and Simpson, 2001; Brocher et al., 2017). The SHZ could possibly represent a localized terrane boundary related to the accretion of Siletzia, and a zone of weakness in the crust which would allow magma to ascend and erupt at a volcano such as MSH (Weaver et al., 1987).

Previous geophysical studies of the region have included detailed passive (Lees and Crosson, 1989; Lees, 1992; Moran et al., 1999; Waite and Moran, 2009; De Siena et al., 2014; Flinders and Shen, 2017; Wang et al., 2017) and active (Parsons et al., 1998; Kiser et al., 2016) seismic tomography and magnetotelluric imaging (Stanley et al., 1987; Egbert and Booker, 1993; Hill et al., 2009). Additional larger-scale studies have been performed in the region using USArray data, including ambient-noise (Gao et al., 2011; Porritt et al., 2011) and teleseismic (Wagner et al., 2010; Schmandt and Humphreys, 2011) tomography, and magnetotelluric imaging (Bedrosian and Feucht, 2014; Meqbel et al., 2014). These types of studies have shed some light on the crustal structure of the region. Using a much denser and wider broadband seismic array than previous experiments, we obtain a high-resolution image of the 3-D crustal

velocity structure in a 50-km radius around MSH from the surface to 20 km depth, using local earthquake tomography. This includes *S*-wave velocity structure, which has not been interpreted extensively at the local level in the region. Further knowledge of the upper crustal velocity structure helps us to understand the geologic history of the region, and provides more context for seismicity and volcanic activity in the area.

In our 3-D local earthquake tomographic models we find good correspondence between the mapped early-Miocene granitic plutons and high-velocity zones which extend to 3-4 km below sea level, and sedimentary rocks of the Chehalis basin and Morton anticline which extend to 6-7 km below sea level. This correlation with local geology is an important indicator that our model is sensitive to shallow crustal lithology and can therefore be used with some confidence to interpret deeper features. At greater depths we find evidence of terrane boundaries, packages of sedimentary rocks, and/or zones of weakness within the middle crust along the SHZ and to the north and northeast of MSH, delineated by low *Vp* and *Vs*. We image a large, low-*Vp* region along the main Cascade arc between Mounts Adams and Rainier at depths of 10-20 km below sea level, which likely corresponds to the hot arc crust and the presence of partial melt. Finally, we image a low-*Vp* and low-Vs region beneath MSH at depths of 6-15 km below sea level that corresponds well with previous geophysical images, earthquake locations, and petrologic results, and is likely delineating a mid- to upper-crustal magma storage region beneath MSH.

3.2. Data

The imaging Magma Under St. Helens (iMUSH) experiment involved multiple geophysical techniques as well as a petrology component, with an aim to illuminate the magmatic system beneath Mount St. Helens. Data for the passive seismic portion of this study

included seismograms from 70 broadband seismic stations deployed from June 2014 to August 2016. Each site contained a Guralp CMG-3T seismometer recording data at 50 Hz to a RefTek RT-130 datalogger, and 94% of total possible data were recovered (Table 3.S1). The diameter of the array was ~100 km, with 10 km average station spacing (Figure 1).

First arrival travel times for *P*- and *S*-waves from 399 local earthquakes with M 0.5-3.0 were recorded at the iMUSH broadband stations, yielding ~10,500 *P*-wave arrivals and ~5600 *S*-wave arrivals. These earthquakes were generally at depths shallower than 20 km and spanned the study area, although they were concentrated to longitudes west of MSH. We also included *P*-wave arrival times on our array from 23 shots set off in 2014 that were part of the active-source component of iMUSH (Kiser et al., 2016), as well as *P*-wave arrival times recorded at 900 Nodal stations deployed in the summer of 2016 (Hansen and Schmandt, 2015).

These data were supplemented with catalog *P*-wave travel times from the Pacific Northwest Seismograph Network (PNSN) for 63 earthquakes with the most travel times recorded on the iMUSH broadband array during 2014-2016. *S*-wave travel times from the PNSN catalog were not used since most PNSN instruments only have a vertical component, and *S*-wave uncertainties are generally harder to evaluate. To obtain a spatially broader *Vp* model, we also used *P*-wave travel times recorded by the PNSN for 205 earthquakes since 2009 corresponding to earthquakes bigger than M2 and recorded by 10 or more stations. This yielded an additional ~6300 *P*-wave travel times. Uncertainties for PNSN travel times follow a similar distribution as the iMUSH broadband data.

We also supplemented our inversion dataset with arrival-time picks from two other temporary deployments: 1) We incorporated 639 *P*-wave and 432 *S*-wave travel time recordings which we made from a 20-broadband array deployed by AltaRock Energy above the SHZ for 5

months in 2016. These travel times came from 46 earthquakes, 29 of which were also recorded on the iMUSH broadband array. 2) We also incorporated ~3600 *P*-wave arrival times from the 1995 Parsons et al. (1998) wide-angle seismic experiment, part of which ran along the Cowlitz River valley to the north end of the iMUSH broadband array.

Arrival times recorded as part of this paper were initially determined using automatic detection and location algorithms that were part of the Antelope software package (see Data and Resources). All arrival times were subsequently reviewed and manually adjusted. Only vertical channels were used for *P*-wave arrival time picks, with horizontal channels used for *S*-wave picks. When *S*-wave arrivals were not simultaneous on both horizontal components (due to shear-wave splitting), we used the earliest *S*-wave. Travel time uncertainties were determined manually and were generally between 0.03-0.15s for *P*-waves and 0.03-0.3s for *S*-waves, with median values of 0.04s and 0.10s, respectively. A minimum of 6 recording stations were required to use an earthquake in the analysis.

3.3. Methods

3.3.1. Methods summary

We invert for 3-D seismic velocity structure using the program struct3dp written by Robert Crosson and based on previous codes used by Symons and Crosson (1997) and Preston et al. (2003). Struct3dp is an iterative, non-linear, conjugate gradient, least squares inversion code with a finite-difference 3-D eikonal equation solver (Vidale, 1990; Hole and Zelt, 1995). Hypocenter relocation is included in the inversion using Levenburg-Marquardt damping. The inversion is regularized using a 3-D Laplacian smoothing operator. We aim to obtain a balance

between smooth model updates and a smooth final model. By adjusting a tradeoff parameter we find a model that minimizes the data misfit as well as the model norm.

3.3.2. Inversion setup

We begin with the initial linearized travel-time inversion problem $A\Delta u + B\Delta h = \Delta t$, where A_{ij} is the ith raypath length in the jth node of the slowness (1/wavespeed) model, u is the vectorized slowness model, B contains the partial derivatives of the travel times with respect to the hypocentral parameters, h represents the hypocentral parameters, and Δt is the residual between the observed and predicted arrival times. In this formulation Δu and Δh are the difference between the updated slowness and hypocenter vectors, u and h, and their values at the previous iteration, u_0 and h_0, respectively. We also incorporate the uncertainties of the travel-time observations into both sides of the equation with the matrix W, which contains the inverse of the travel-time pick uncertainties ($1/\sigma_i$) along the diagonal.

To regularize the problem we introduce a Laplacian operator, L, which acts to smooth the model in each spatial dimension. We can control the vertical versus horizontal shape of the smoothing in this step to be between an isotropic filter and one that enforces little or no vertical smoothing. In the models shown we use a value of 0.7, where 0 makes an isotropic filter and 1 enforces zero vertical smoothing. This allows the velocity to vary more vertically than horizontally, while still enforcing some vertical smoothness. We also introduce a smoothing tradeoff parameter λ (Figure S3) and a parameter η which can be varied between 0 and 1 and controls whether an inversion run is optimized for smooth model perturbations or a smooth final model. Since $u = u_0 + \Delta u$ and Lu gives the roughness of a given slowness model, the second part of our equation varies between minimizing the roughness of model perturbations $L\Delta u = 0$ ($\eta =$

0) and minimizing the updated slowness model, u: $Lu = 0 = Lu_0 + L\,\Delta u$ ($\eta = 1$). We choose a value of η equal to 0.5 to balance between smoothing model perturbations versus the final model. We also minimize the perturbation to the hypocentral parameters using Levenberg-Marquardt damping H, where H contains values of 0.3 km^{-1} for the hypocentral parameters and 0.075 s^{-1} for temporal.

$$\begin{bmatrix} WA & WB \\ \lambda L & 0 \\ 0 & H \end{bmatrix} \begin{bmatrix} \Delta u \\ \Delta h \end{bmatrix} = \begin{bmatrix} W\Delta t \\ -\eta\lambda L u_0 \\ 0 \end{bmatrix}$$

We employ the conjugate-gradient least-squares approach to solve this system of equations. Our approach involves 9 major iteration loops, with 9000 to 12000 model updates in each.

3.3.3. Starting velocity models

Our starting *P*-wave velocity model was initially a combination of the PNSN "C3" and "S4" velocity models, which are 1-D models used by the PNSN for the Washington Cascades and the MSH areas, respectively (Leaver et al., 1984; Malone and Pavlis, 1983). Ultimately, we use an input 1-D *Vp* model which is made up of the average velocity of a previous 3-D model at each model node depth within 30 km of MSH (Figure 8). The previous 3-D model inversion was performed using a smaller dataset with only the first half of the iMUSH broadband array data. Similarly, we tested a variety of input Vs models, including the average of a previous model at each depth, our starting *Vp* model divided by 1.73, or the PNSN 1-D models divided by 1.73. After testing multiple input velocity models we found that inversion results did not depend strongly on the starting model, except for near the model edges where there are not any seismic

raypaths to constrain the inversion. In particular, the major interpreted below were not impacted by different starting models.

The velocity models presented in this paper are defined with 195x200x55 nodes in east, north, and down directions, with 1.2 km spacing in all directions. The grid origin is at 123.7W and 45.2N and 5 km above sea level.

3.3.4. Earthquake relocation

Earthquake hypocenters input into the inversion are PNSN catalog locations when available, and Antelope-derived locations otherwise. The inversion uses Levenburg-Marquardt damping. On average, earthquakes are relocated 1.0 km from the initial location, with >96% of the relocation distances less than 2 km. The root-mean-square (RMS) travel-time residual is reduced from .316s in the initial 1-D *Vp* model to .057s in the final 3-D *Vp* model. In the Vs inversion the RMS travel-time residual is reduced from .480s to .046s (Figure S4).

3.3.5. *Vp*/Vs, or best approximation with matched raypaths

In addition to the separate *Vp* and Vs inversions, which we perform with the maximum possible number of respective arrival times, we also perform *Vp* and Vs inversions with matching source-receiver pairs. In doing so, we attempt to minimize the difference in resolution between the separate inversions so that a comparison of *P*- and *S*-wave velocities is more robust. In these matched inversions, the input data set is limited to 4575 arrival times from 328 earthquakes recorded at 97 stations.

3.3.6. Resolution testing

We perform resolution tests on the model inversion using a 'checkerboard' scheme (Spakman and Nolet, 1988). With the checkerboard test, we impose a 10% 3-D sinusoidal velocity perturbation to our best-fit 3-D model, calculate predicted arrivals through this model, add random Gaussian noise with the same standard deviation as the actual travel-time residuals, and then invert the synthetic data to see how well we recover the perturbed model. In addition, we perform semblance tests based on the methodology of Zelt (1998), which uses 16 offset checkerboard patterns to determine how well variations are recovered at each model node (see Supplementary Materials for details).

In addition to the checkerboard tests for the entire model area, we perform resolution tests with applied velocity anomalies beneath MSH intended to approximate a magma storage region (Figure 6). We apply perturbations to our best-fit 3-D velocity model with Gaussian distributions in all three spatial dimensions, centered at 10 km beneath MSH. We set vertical standard deviation of the perturbation to 4 km for all input models, and horizontal standard deviations to 1, 2, and 4 km. We also apply amplitude variations of -10 and -20%. This results in six different input perturbations (Table 3). Similarly to the checkerboard tests, we calculate predicted arrivals through the perturbed model, add random Gaussian noise to those arrivals, and invert the synthetic data set to see how well we recover the perturbed model.

3.3.7. Results of resolution testing

Using checkerboard resolution testing, we can resolve features in the *Vp* model with 5-km width to depths of 15 km, and features with 20-km width to depths of 25 km (Figure 3.S1 and Figure 3.S2). Amplitude reductions in the resolved model are on the order of 5-40% relative

to input models, with the reductions generally larger for negative perturbations. The best resolved areas are within the footprint of the iMUSH broadband array, although there are some additional well-resolved areas to the SW and NE. In the Vs model we can resolve features of 5-km width to depths of 13-14 km only in the NW section of the broadband array footprint, and features with 20-km width to depths of 20 km. Amplitude reductions are similar to those for the *Vp* model. For both the *Vp* and Vs models, resolution is better in the western side of the broadband array, especially to the northwest. This is likely due to the concentration of seismicity and instrumentation in that area.

Beneath MSH, our resolution for features approximating a magma storage region varies depending on the spatial size of the input anomaly and the amplitude of the perturbation (Figure 6; Table 3). The input perturbation which results in an output most similar to our actual 3-D model is a 10% velocity reduction with a radius of 2 km. An input anomaly with radius of 4 km would be recovered very well, and since we do not see a similar pattern in the 3-D model, it is unlikely that there is a low-velocity region of that size. We do not recover 1-km-radius input anomalies, so it is possible that there is a narrow region with very high velocity perturbation that we are unable to image with our methodology and station geometry. Increasing the perturbation amount decreases the relative amplitude recovery, likely due to raypaths being bent around the large velocity anomaly in the forward modeling.

3.4. Results

3.4.1. Shallow velocity variations

We find several high-velocity anomalies near the surface throughout the region, in both the *Vp* and Vs models (Figure 2). These areas have a maximum 15-30% faster *P*- and *S*-wave

velocity, corresponding to 5.8-6.4 and 3.3-3.8 km/s, respectively. The dimensions of the anomalies range from 5-20 km wide and extend to 3-4 km depth below sea level.

There are three major low-velocity anomalies in the *Vp* model near the surface (Figure 2). The largest anomaly begins 30-40 km NW of MSH, and extends to the SW, NW, and NE from there. Negative velocity variations exceed 20%, with *Vp* and Vs speeds of less than 3.6 and 2.2 km/s, respectively. This low *Vp* and Vs region extends to depths of around 7 km below sea level. To the east of there and north of MSH, near the Cowlitz river, is another low velocity region, with maximum anomalies of -19% for *Vp* and -11% for Vs, corresponding to speeds of 4.10 and 2.60 km/s. This feature also extends to depths of approximately 7 km below sea level. The third major negative velocity anomaly near the surface in both models is near the Indian Heaven volcanic field to the SE of MSH, with maximum anomalies of 15-20% for *Vp* and Vs, corresponding to 4.25 and 2.34 km/s, respectively. This feature extends to depths of ~3 km below sea level.

The Vs model has an additional shallow low-velocity region that is not as pronounced within the *Vp* model, situated approximately between Indian Heaven and the area just to the WSW of MSH. This leads to one of the primary high *Vp*/Vs ratio areas within the study region.

3.4.2. Mid-crustal velocity variations

We image low velocities along the Mount St. Helens seismic zone (SHZ; Figure 3), a region of elevated seismicity running NNW-SSE through MSH (Weaver et al., 1987), which shows focal mechanisms consistent with right-lateral strike slip faulting. The low velocities in *Vp* and Vs extend in a several-km-wide section from near the surface to depths of 15-20 km, the maximum resolvable depth in our model. Average anomalies range from 3-5% below average

(Figure 4). At shallow depths, above 2-3 km below sea level, the *S*-wave velocities are notably lower, contributing to a high *Vp*/Vs ratio.

We find a low *P*- and *S*-wave velocity region at depths of 6-15 km below sea level beneath Mount St. Helens (Figure 5). This region is on average 3-5% below the surrounding velocity, with a width of 5-6 km. Based on resolution testing, the anomaly could also be produced by inaccuracies in the inversion if the actual anomaly were closer to 10% negative velocity and a width of 4 km (Figure 3.6; Table 3.5). The shape of the anomaly in both the *Vp* and Vs models is very similar, even though the data sets are independent and were inverted separately.

A broad low-*Vp* region is apparent stretching from Mount Adams to Mount Rainier at depths of 10-20 km below sea level, with >10% change in velocity from the surrounding area (Figure 7). Our resolution is limited in this portion of the model due to fewer raypaths (due to fewer earthquakes and stations in the eastern part of our study area), but the spatial dimension and velocity perturbation of the anomaly is great enough to still be resolvable as seen in our semblance testing at 20-km scale lengths (solid black contour in Figure 7). There is no Vs data available for this portion of the study area.

3.5. Discussion

3.5.1. Shallow

3.5.1.1. Early Miocene plutons

Many or all of the high-velocity anomalies in the *Vp* and Vs models at shallow depths correspond to plutonic rocks mapped at the surface, including the Oligocene to Miocene-aged Spirit Lake (Evarts and Ashley, 1984; Evarts et al., 1987), Spud Mountain, Tatoosh (Fiske et al.,

1963; Mattinson, 1977), and Silver Star plutons (Felts, 1939), and the intrusive rocks of McCoy and Kidd Creeks (Link, 1985; Swanson, 1992; Hagstrum et al., 1998). These plutonic rocks exposed at the surface are predominantly granitic, and the seismic velocities (*Vp* 6.0-6.4 km/s) we measure match laboratory experiments for granite at temperatures and pressures expected near the surface (Christensen, 1979; Christensen and Mooney, 1995).

Previous geophysical studies have also imaged some of these features with varying degrees of resolution. By making use of the iMUSH broadband station spacing, we provide consistent constraints on the size and depth of these anomalies, especially those further from MSH that have not been analyzed by previous studies. In all cases the total area covered by the high velocity regions is larger than the area indicated by surface exposure.

The Spirit Lake and Spud Mountain plutons to the north of MSH have been extensively imaged by previous geophysical studies, including local earthquake tomography (Lees and Crosson, 1989; Moran et al., 1999; Waite and Moran, 2009), ambient noise tomography (Flinders and Shen, 2017; Wang et al., 2017), active source tomography (Kiser et al., 2018), magnetotellurics (Bedrosian et al., 2018), gravity (Williams et al., 1987) and magnetic (Finn and Williams, 1987) surveys. In our *Vp* and Vs models, the high-velocity anomalies associated with these plutons extend from the surface to depths of 3-4 km below sea level, signifying volumes on the order of 1000 km^3. It is possible that the plutonic rocks extend deeper than 3-4 km, as the absolute velocities remain at similar values. However, the velocity anomalies at that depth are greatly diminished as the surrounding rocks could have similar seismic velocities.

Two smaller high-*Vp* anomalies at shallow depths to the south of MSH also correspond to unnamed Tertiary intrusive rocks which outcrop to the west of the Cinnamon Peak andesite and Marble Mountain basalt/andesite flows (Evarts et al., 1987), respectively. These anomalies do

not appear in the 3-D Vs model, perhaps due to issues with resolution. However, there is a high-Vs anomaly to the west of Marble Mountain imaged by ambient noise tomography using the dense iMUSH Nodal array (Wang et al., 2017). A local earthquake tomographic study by Lees and Crosson (1989) also imaged high-velocity features in the region to the south of MSH. Williams et al. (1987) analyzed a gravity high near Cinnamon Peak and Marble Mountain and inferred the anomaly to be due in part to an intrusive complex that extends beneath MSH. We note that our 3-D velocity model shows high velocity anomalies in this area, consistent with intrusive rocks.

The 10-km-wide high-velocity region 40 km to the WSW of MSH does not correspond to a surface-mapped pluton. The area it is in was an Eocene-Oligocene basaltic-andesite flow member of the Goble Volcanics, thought to be ~1500 meters thick (Phillips, 1987; Smith, 1993). Perhaps there is a crystalline pluton beneath the lava flow of a similar size and type as the Spud Mountain and Spirit Lake plutons. There is also a relative gravity high in that location (Finn et al., 1991), and it was possibly imaged by other geophysical studies (Moran et al., 1999; Kiser et al., 2018; Bedrosian et al., 2018).

Approximately 30 km to the ENE of MSH there is an additional high-velocity anomaly in the *Vp* and *Vs* models, which corresponds with the intrusive suite of Kidd Creek and the McCoy Creek quartz diorite (Swanson, 1992). Swanson (1992) discussed this system of radial dikes and sills as being the roots of a Miocene volcano, the top of which has since been eroded. This pattern of intrusive rocks beneath a volcano may be similar to the high *P*-wave velocities (our study) and gravity anomaly seen beneath MSH (Williams et al., 1987).

3.5.1.2. Sedimentary basins

The large low-velocity feature at the western and northwestern edges of the model area corresponds to the Chehalis sedimentary basin, which is thought to be made up of alternating layers of sedimentary and volcanic rocks, from the Eocene to Quaternary, and underlain by Siletzia basalts at 5-6 km depth (Stanley et al., 1994). Travel-time delays recorded here exceed 1 s. The low-velocity anomaly extends to 8 km depth, although at this end of the model there are not enough source-receiver raypaths included to fully resolve the depth and shape of the anomaly. This sedimentary basin has also been imaged with active source seismic tomography (Parsons et al., 1998; Kiser et al., 2016), magnetotellurics (Stanley et al., 1994), and magnetic and gravity anomalies (Finn, 1990).

Another low-velocity near-surface anomaly extends eastward from the Chehalis basin towards the middle- to upper-Eocene Puget Group sediments outcropping at Bear Canyon and the Morton anticline (Schasse, 1987; Stanley et al., 1996), to the north of Mount St. Helens. This feature extends to depths of approximately 7 km was also mapped by the active source profile by Parsons et al. (1998).

3.5.1.3. Indian Heaven and south of MSH

The area around the Indian Heaven volcanic field shows a low-velocity trend in both the *Vp* and *Vs* models, with anomalies >15% negative. This area is made up of dozens of Quaternary-aged basaltic and andesitic vents that total ~70 km^3 of eruptive material (Korosec, 1989; Hildreth, 2007). These were erupted within a large, N-S striking syncline made up of rocks of the Western Cascades Group (Hammond, 1979; Mitchell, 1989) that formed between the Eocene and Miocene and consist of andesite and basalt flows, tuffs, mud flows, and

volcaniclastic deposits. The region has been highly fractured, hosting numerous faults and igneous intrusions (Mitchell, 1989; Korosec, 1989). We infer that this faulting and fracturing could be the source of the low velocities in the area.

In both the *Vp* and *Vs* models there is an extension of this low-velocity region towards the south of MSH, although the low-velocity anomaly is much stronger in the *Vs* model 10 km to the south of MSH. This difference between the *Vp* and *Vs* models is more pronounced in the full data inversions than in the 'matched raypath' inversions, so the magnitude of the anomaly could be partly due to a resolution issue. For example, there is a high velocity region in the *Vp* model in the top 2-3 km 10 km SSE of MSH (discussed in section 3.5.1.1) which does not appear in either *Vs* model or the 'matched raypath' *Vp* model. However, there is still a high *Vp*/*Vs* anomaly regardless of the matched or full models compared. This anomaly could be related to increased hydrothermal fluid circulation within the upper 2-3 km in this region.

3.5.2. Mid-crustal

3.5.2.1. St. Helens seismic zone

The low velocities imaged in the *Vp* and *Vs* models along the Mount St. Helens seismic zone (SHZ) could represent a region of elevated temperature, fractured rock, or fluids. Another possibility is the presence of sedimentary rocks, which are exposed to the north in the Morton anticline and could be left over from the suture of the Siletz terrane onto the North American continent around 55-50 Ma (Stanley et al., 1987; Bedrosian and Feucht, 2014). As Weaver et al. (1987) noted, the faulting along this region is a potential means for accommodating crustal shortening experienced by southern Washington State due to the northward rotation of the Oregon crustal block (Wells et al., 1998). The resulting fracturing and/or the existence of

sedimentary rocks or other terrane boundary at depth would create a zone of weakness that could be exploited by magma and fluids rising from the lower crust, potentially providing an explanation for why MSH is located where it is. The presence of fluids within the top few km would also help to explain the high *Vp*/*Vs* ratios that we image near the surface at the SHZ between the Spud Mountain and Spirit Lake plutons.

The SHZ is aligned with the western edge of the magnetotelluric anomaly termed the SWCC (Stanley et al., 1987; Egbert and Booker, 1993; Hill et al., 2009). Recent high-resolution magnetotelluric images (Bedrosian et al., 2018) show that the highly conductive rocks are concentrated in and along the SHZ, in the same location as seismicity and our low velocities. Previous earthquake tomography studies have also imaged low *P*-wave velocities along the SHZ (Lees and Crosson, 1989; Moran et al., 1999; Waite and Moran, 2009), and De Siena et al. (2014) found a high-scattering and high-attenuation anomaly in the same area, which is consistent with the presence of sediments. We believe the geophysical evidence and our new observation of low *S*-wave velocities supports the idea proposed by Stanley et al. (1987) and others (Moran et al., 1999; De Siena et al., 2014) that this area is made up of marine and/or continental sedimentary rocks associated with the accretion of Siletzia.

Perhaps coincidentally, the SHZ is directly above the eastern edge of the inferred serpentine mantle wedge (Hansen et al., 2016). One potential explanation is that a warm mantle wedge such as that associated with subduction of the young and warm Juan de Fuca plate would release fluids (water) along a line directly below the trace of the SHZ (Kirby et al., 2014). Thermal models for the warm Cascadia subduction zone indicate that a serpentine mantle wedge may be bounded on top by the continental crust, on the bottom by the subducting oceanic crust and on the east by the 700 degree isotherm that marks the stability field for serpentine (Hansen et

al., 2017). The Juan de Fuca plate velocity in the vicinity of Mount St Helens has been cut roughly in half during the last 7 Ma with respect to the Hot Spot reference frame (from 46 to 18 mm/a) or with respect to North America (from 68 to 40 mm/a) (Riddihough, 1984; D Wilson, 1993). Though we have not run thermal models for this particular subduction history, we would expect that the slowing subduction rate would produce a time-dependent heating of the subducting plate leading to slight heating of the wedge, which in turn would release water along the eastern edge of the wedge where serpentine is at its stability temperature. This is supported by thermal models for California that start with steady-state subduction followed by stopping subduction all together and produce a well-developed serpentine mantle wedge that slowly heats up by conduction (Kirby et al., 2014)

3.5.2.2. MSH magma storage

The low-*Vp* and low-*Vs* anomaly beneath MSH at depths of 6-15 km is in a similar location as previously imaged low-*Vp* anomalies (Lees and Crosson, 1989; Lees, 1992; Moran et al., 1999; Waite and Moran, 2009), as well as a high-conductivity region imaged by magnetotelluric methods (Hill et al., 2009; Bedrosian et al., 2018) and within a zone of seismic activity (Scandone and Malone, 1985; Barker and Malone, 1991). This all points to the possibility of it being a shallow magma storage region. Based on the size and amplitude of the velocity anomaly in our models, it could contain 5-10 km^3 partial melt (Watanabe, 1993) in a 250 km^3 volume. This amount of partial melt does not vary significantly if we consider higher amplitude, narrower anomalies such as was done in our resolution testing, since the effects offset each other. It is also similar to previous estimates of a magma chamber volume beneath MSH using seismicity. Barker and Malone (1991) described a volume of 5-7 km^3 at 7 to 11 km depth

using a change in stress field from earthquake focal mechanisms, while Scandone and Malone (1985) found an earthquake-free volume at 7-14 km depth with a minimum volume of 10 km^3. This volume of partial melt is about 2 times larger than the largest previous eruption at MSH, which had an estimated volume of 3-4 km^3, occurred ~3400 years ago and is marked by the Yn tephra deposit (Mullineaux, 1996).

We do not image a low-velocity region at depths of 2-3 km beneath MSH, which Waite and Moran (2009) imaged in *Vp* and inferred was a shallow magma storage area. One possible difference is the methods used between the two studies. They used a ray-shooting algorithm to calculate travel times, whereas we used finite difference ray tracing. The main difference between these two methods is that the eikonal solver will find the fastest raypath and includes headwaves and diffracted waves, while ray shooting may find later arriving rays, which would lead to an interpretation of low velocities.

Compared to the broader low-velocity region near Mounts Adams and Rainier, this anomaly beneath MSH is much smaller spatially and in velocity perturbation; perhaps because MSH is located so far to the west of the main volcanic arc it lacks the extensive heating and magmatic intrusion within the crust of the main volcanic arc.

3.5.2.3. Slow subarc mid crust

The broad low *Vp* zone stretching between Mount Adams and Mount Rainier is possibly part of the main arc crust, where we would expect to see higher temperatures and the presence of partial melt. The placement of the anomaly also agrees with low-*Vp* measured by Moran et al., (1999) and partially with low-*Vs* measured by Obrebski et al. (2015) and Flinders and Shen (2017). Heat flow measurements indicate a peak at over 80 mWm^{-2} along the axial region from

Indian Heaven to Mount Adams to Goat Rocks. Mounts St. Helens and Rainier lie on the western and northern edges of this high heat flow area, respectively, with heat flows closer to 50 mWm^{-2} (Blackwell et al., 1990). Temperature alone, however, is not enough to account for the low *Vp* values in the model. The presence of ~10% partial melt would be enough to lower the seismic velocity to the values that we see (Watanabe, 1993), although the placement of the center of the anomaly 20-km to the east of the main arc may require a different explanation. It is possible that the low velocities are instead related to a change in crustal composition or extensive fracturing (as postulated by Obrebski et al., 2015) related to the Mesozoic subduction mélange outcropping at the Rimrock Lake inlier (Miller, 1989) near White Pass.

Although there are fewer raypaths in the region of this anomaly, it is wide enough and high-amplitude enough that we believe it is still resolved. We performed semblance testing on a larger model with checkerboard wavelengths of 40 km, and this region fell above the 0.7 contour for semblance, indicating that it is sufficiently resolved at this scale.

3.5.3. Additional seismic structures

Additional low-velocity regions in the middle crust to the NE of MSH near the Skate Mountain anticline, could also correspond to the marine and non-marine sediments deposited in the area during the accretion of Siletzia, similar to those at the Morton anticline. These correspond spatially to the eastern edge of previously imaged low-resistivity rocks which were termed the Southwest Washington Cascades Conductor (SWCC; Stanley et al., 1987). Based on recent high-resolution MT results (Bedrosian et al., 2018) the low-resistivity, high-conductivity rocks make up a narrower band, or ring, stretching from MSH along the SHZ, and moving eastwards towards Goat Rocks, then south to the west of Mount Adams. We interpret the

presence of low-velocities and high-conductivities to indicate the presence of these sediments, providing more evidence for the tectonic history of accretion in the region.

While we potentially image sediments deposited during and after the accretion of Siletzia in the area between MSH and the main Cascade arc, we do not see a definitive boundary of the high-velocity gabbros which we would expect to image from the lower crustal portion of the Siletz terrane. In our larger scale *Vp* inversion we image a region at 10-20 km depth near the mouth of the Columbia River which has velocities greater than 7 km/s, which you would expect for gabbro (Figure 7; Christensen and Mooney, 1995). However, these high velocities do not extend further east towards MSH. Instead, in the upper-middle crust (10-20 km), we image some areas ranging from 6.6-6.9 km/s, and others from 6.3-6.5 km/s, which are more consistent with low-grade metamorphic basalt (Christensen and Mooney, 1995). This transitional region between the high velocities near the mouth of the Columbia and the low velocities along the SHZ and beneath MSH lies near the proposed Siletzia boundary inferred from magnetic data by Wells et al. (1998).

3.6. Conclusions

We provide supporting evidence using 3-D *Vp* and *Vs* models for several broad interpretations of the geologic setting and tectonic history of the Mount St. Helens (MSH) area. The largest anomalies in our seismic velocity models occur near the surface, and correlate very closely with geological features mapped at the surface, including many Miocene-aged plutons, Quaternary-aged and Tertiary-aged sedimentary basins and units, and the Indian Heaven volcanic field. At depths of 5-15 km, we see low *Vp* and *Vs* along the Mount St. Helens seismic zone, which corresponds very closely with high conductive anomalies, indicating the possible

presence of fluids and sedimentary rocks from the accretion of the Siletz terrane. This correspondence between low velocities and high conductivities continues towards the east, essentially framing the edge of the previously imaged Southwest Washington Cascades Conductor (SWCC). Beneath MSH, we image low *P*- and *S*-wave velocities at 6-15 km depth, in a roughly cylindrical shape, which could indicate the presence of a narrower zone of partial melt storage beneath the volcano, possibly holding up to 5-10 km^3 of partial melt. Finally, we image a large, low *Vp* region at depths of 10-20 km in the mid-crust beneath and to the east of Mount Adams and stretching towards Mount Rainier. This area is likely host to higher temperatures and some amount of partial melt associated with the primary magmatic axis in this region of the Cascades.

3.7. Supplementary material

3.7.1. Model evaluation

Model fit is measured by using the weighted travel time rms (*i* refers to each observation):

$$\left(\sum_i^n \frac{\sigma_{ref}(t_i - t_{src_i} - tt_{calc_i})^2}{\sigma_i}/n\right)^{1/2}$$

Raw travel time rms:

$$\left(\left[\sum_i^n (t_i - t_{src_i} - tt_{calc_i})^2\right]/n\right)^{1/2}$$

Model roughness is evaluated as:

$$(Lu)^T Lu$$

3.7.2. Semblance testing

We perform semblance tests on our input and recovered checkerboard patterns (Figure S1) to determine the resolution of various-sized features from the inversion, based on the methodology of Zelt (1998). The semblance *S* for a specific model node is defined as

$$S = \frac{\sum_{j=1}^{N}(P_{t_j} + P_{r_j})^2}{2 * \sum_{j=1}^{N}(P_{t_j}^2 + P_{r_j}^2)}$$

where P_{t_j} and P_{r_j} are the true and recovered velocity perturbations at the *j*th node inside a spherical volume consisting of *M* nodes around the center node. The spherical volume has a radius of 5km. The semblance varies from 0 to 1, where 0 is perfectly anti-correlated and 1 is perfectly correlated. We use a value of $S>0.7$ to indicate good recovery of the input checkerboard perturbation, based on the results of Zelt (1998).

Since checkerboard perturbation recovery can vary depending on whether the perturbation is at a positive or negative maximum or 0, we use multiple input checkerboards with the perturbation origin shifted for each one. We use a total of 16 input checkerboards, 8 of which are shifted 0 or ¼ wavelengths in the x-y-z directions from the original (making the vertices of a cube with side length = ¼ wavelength), and the remaining 8 which are ½ wavelength (180 degrees out of phase) from the original 8. The ultimate semblance value used for each wavelength of perturbation at a given model node is the average semblance value for each of the 16 input checkerboards (Figure S2).

We calculate semblance values for checkerboard perturbations with wavelengths of 10, 15, 20 and 40 km.

3.7.3. Catalog earthquake relocation

In addition to the ~600 earthquakes relocated during the velocity model inversion, we have relocated ~20000 PNSN catalog earthquakes going back to 1980, by using the best-fit 3-D *Vp* and *Vs* models and using the following method.

We generate travel-time grids for each station that had a PNSN catalog travel time pick for any of the events of interest. Then for each event we perform a grid search over the model area within 10 km of the PNSN location and define the hypocenter misfit at a given node *k* as:

$$M_k = \sum_{i=1}^{n} \frac{(t_{obs_{ik}} - t_{or_k} - tt_{ik})^2}{\sigma_i^2}$$

where M_k is the misfit, $t_{obs_{ik}}$ is the observed arrival time at station *i* for node *k*, t_{or_k} is the hypocenter origin time, tt_{ik} is the travel time from station *i* to grid node *k*, *n* is the number of observed arrival times for the given event, and σ_i is the arrival time uncertainty. To find the best-fitting origin time for an earthquake at this location, we set the derivative of the misfit with respect to t_{or_k} , $\frac{dM_k}{dt_{or_k}}$, equal to zero. After simplification, we obtain

$$t_{or_k} = \frac{\sum_{i=1}^{n} [(t_{obs_{ik}} - tt_{ik})/\sigma_i^2]}{\sum_{i=1}^{n} [1/\sigma_i^2]}$$

Using t_{or_k}, we can calculate the misfit, M_k, at this grid node. After performing this process at each grid node, we find the minimum misfit value to obtain the best-fitting hypocenter for the given event. To improve the location, we repeat the process near the initial location over a finer interpolated grid, with side length equal to 60m. In all cases, we restrict the grid search to be below local land elevation, so that there will not be any "airquakes."

3.7.4. Velocity model format

The velocity models described in this chapter are provided as NetCDF files, with the following dimensions and variables.

Dimensions:

NX – the number of model nodes in the x (E-W) direction
NY – the number of model nodes in the y (N-S) direction
NZ – the number of model nodes in the z (up-down) direction
NCOORDS – 3, for x,y,z
NSRC – the number of sources used
NREC – the number of receivers used
NSLO – the number of model nodes
NOBS – the total number of observations
NAMELEN – name length

Variables:
dx – x node spacing (km)
dy – y node spacing (km)
dz – z node spacing (km)
slo – the slowness (1/velocity) vector (s/km)
sens – sensitivity vector, corresponding to the number and weight of rays traced through each model node
origin – the south, west and top corner of the model grid
srcx – x location of sources, in Cartesian coordinates (km)
srcy – y location of sources, in Cartesian coordinates (km)
srcz – z location of sources, in Cartesian coordinates (km)
srct – time of sources, from arbitrary reference (s)
recx – x location of receivers, in Cartesian coordinates (km)
recy – y location of receivers, in Cartesian coordinates (km)
recz – z location of receivers, in Cartesian coordinates (km)
resid – observed minus predicted arrival time for each observation (s)
uncert – uncertainty of each observation (s)
srcindex – index relating each observation to its source
recindex – index relating each observation to its receiver
srcnames – names of sources
recnames – names of receviers

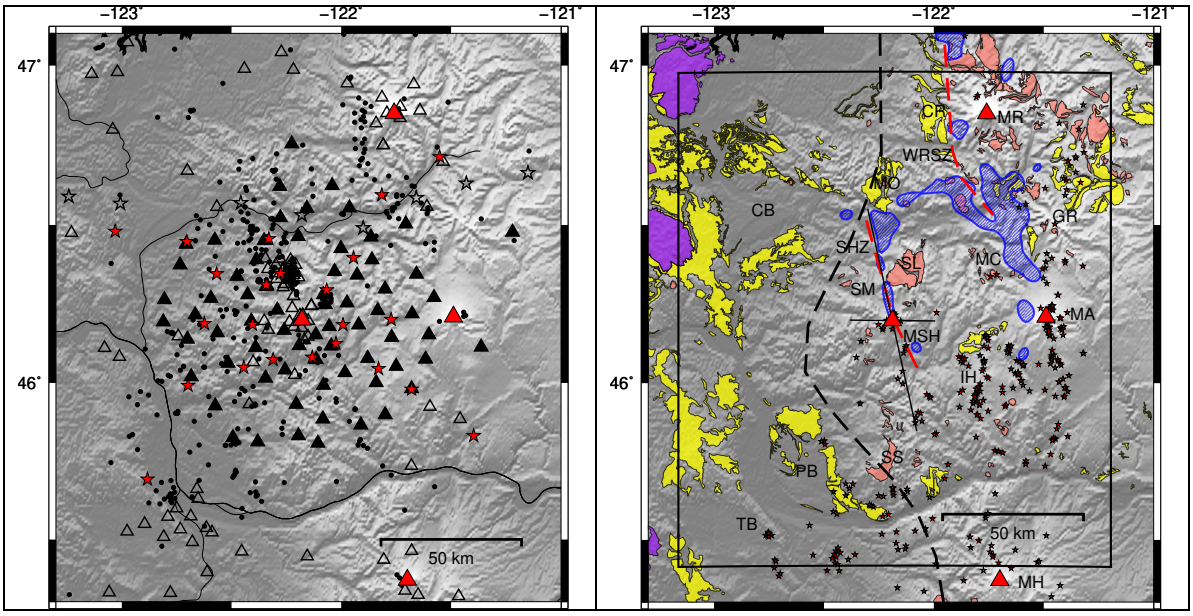

Figure 3.1. Source and station distribution and geologic setting.

A (left). Source and station distribution. Earthquake locations used in the inversion (black dots) and shot locations from Kiser et al. (2016; red stars) and Parsons et al. (1998; black open stars). Broadband iMUSH stations from this project (solid black triangles), plus other permanent and temporary stations (open black triangles). Mounts Rainier, St. Helens, Adams, and Hood denoted by red triangles. **B** (right). Geologic setting of the area. Locations of plutonic rocks (pink), Tertiary sediments (yellow), Siletz outcrops (purple) from Schuster (2005) and Walker and MacLeod (1991); Quaternary vent locations (stars; Hildreth, 2007); and volcanoes (red triangles; labels MR, MSH, MA, and MH for Mounts Rainier, St. Helens, Adams, and Hood). Dashed black line indicates the eastern boundary of the Siletzia terrane inferred from magnetic data (Wells et al., 1998), dashed red lines indicate the Mount St. Helens and West Rainier seismic zones (SHZ and WRSZ). Blue hachured area is the 0.5 $\log_{10}$(resistivity) contour at 8km depth from Bedrosian et al. (2018). CR: Carbon River anticline; MO: Morton anticline; CB: Chehalis sedimentary basin; GR: Goat Rocks; MC: McCoy Creek intrusive complex; SL: Spirit Lake pluton; SM: Spud Mountain pluton; IH: Indian Heaven volcanic field; SS: Silver Star pluton. Black box indicates outline of velocity models shown in Figure 2, and black lines show locations of cross-sections in Figures 3 and 4.

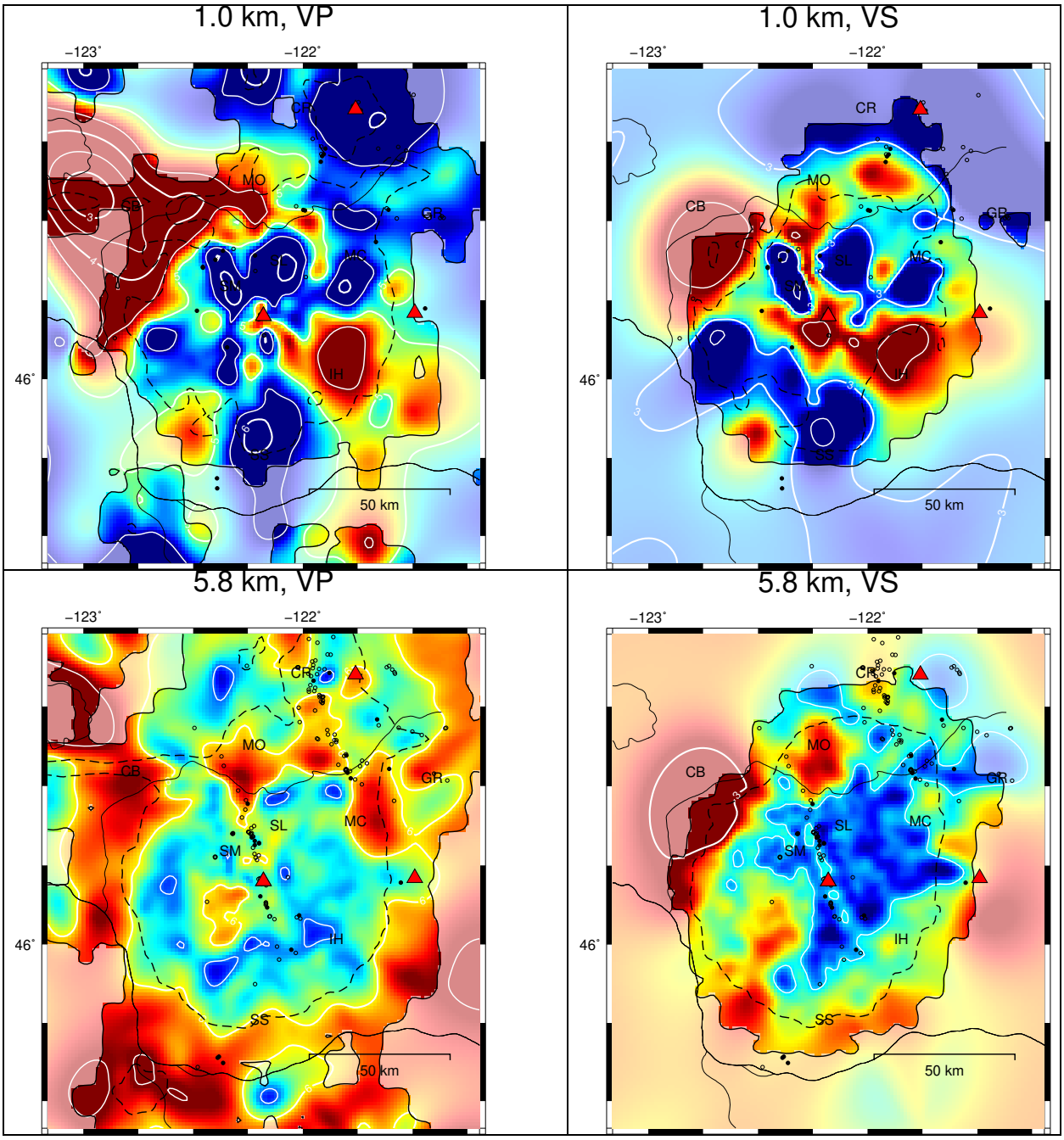
1.0 km, VP
1.0 km, VS
5.8 km, VP
5.8 km, VS
−123˚
−122˚
46˚
CR
MO
CB
GR
SL
MC
SM
IH
SS
50 km

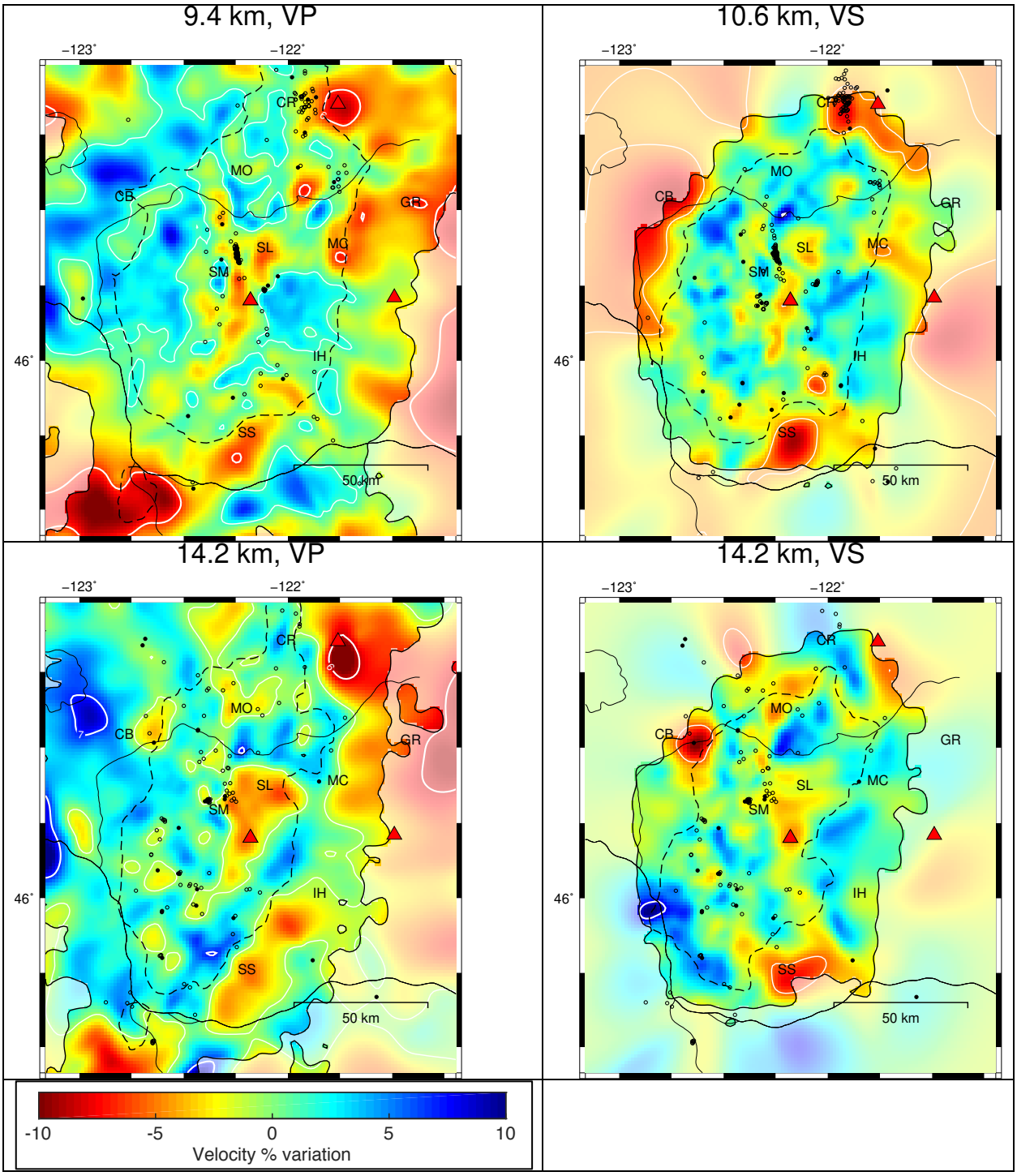

Figure 3.2. *Vp* and *Vs* model depth slices.
Depth slices through *Vp* and *Vs* models at 1.0, 5.8. 9.4, and 14.2 km below sea level, showing percent variation from a 1-D model. White contours show absolute velocity, and dashed black contours delineate the region within a semblance contour of 0.7 for features with 10-km wavelength. Earthquakes used in inversion (filled black circles) and relocated UW catalog earthquakes (open black circles) are also shown. Red triangles indicate position of MSH and Mount Adams, letter codes are the same as in Figure 1B.

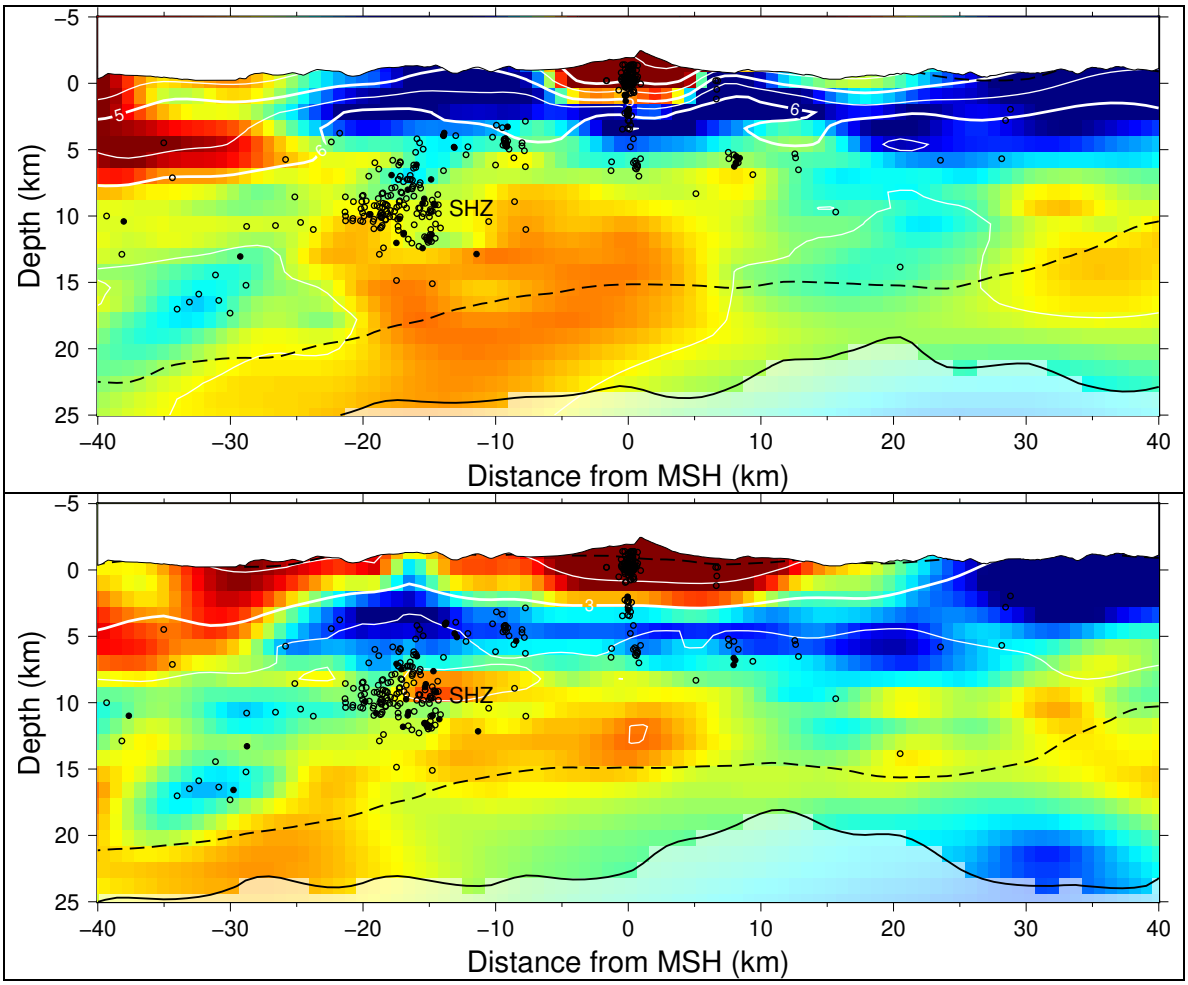

Figure 3.3. *Vp* and *Vs* model cross-sections at SHZ.

Cross-sections through MSH and along the SHZ for the *Vp* (top) and *Vs* (bottom) models. Contours and earthquakes same as Figure 2.

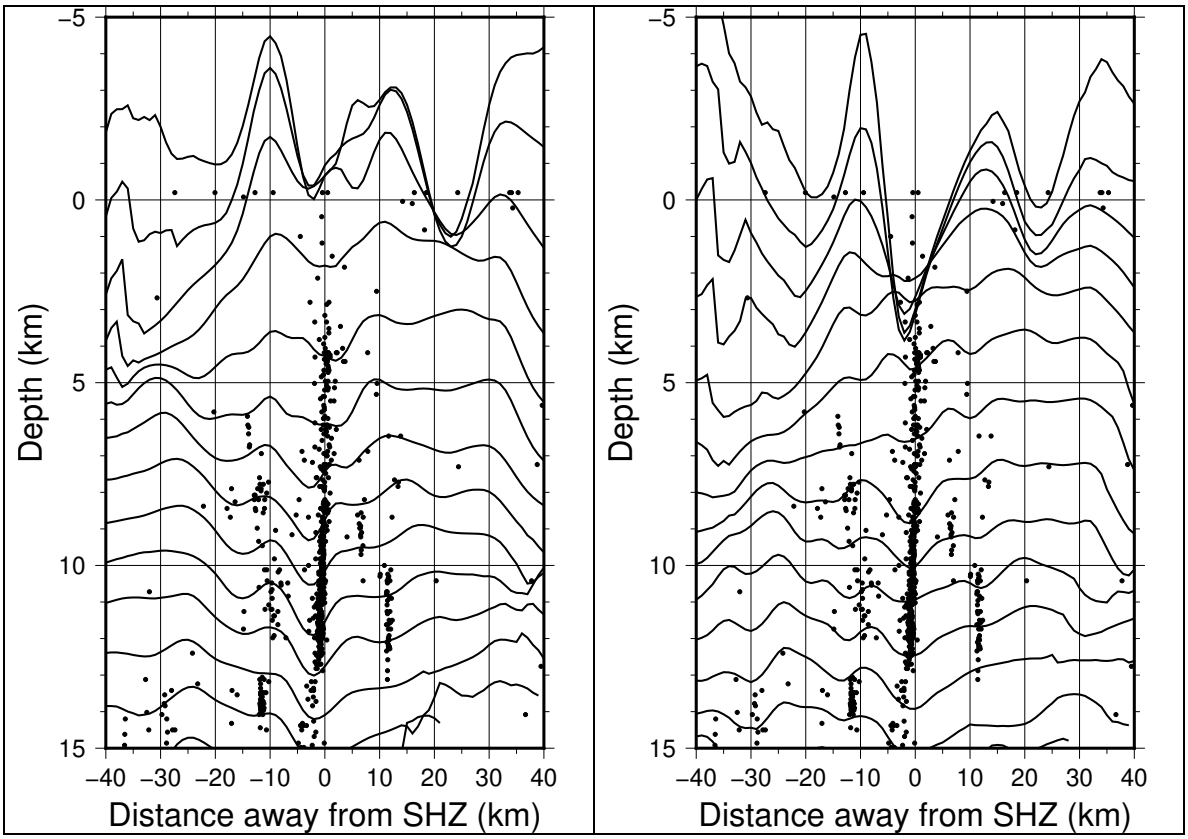

Figure 3.4. Average velocity variations parallel to SHZ.

Average velocity variations parallel to the SHZ for the *Vp* (left) and *Vs* (right) models. Earthquakes within 40 km (excluding those directly beneath MSH) are projected to the plane perpendicular to the SHZ and plotted as black dots.

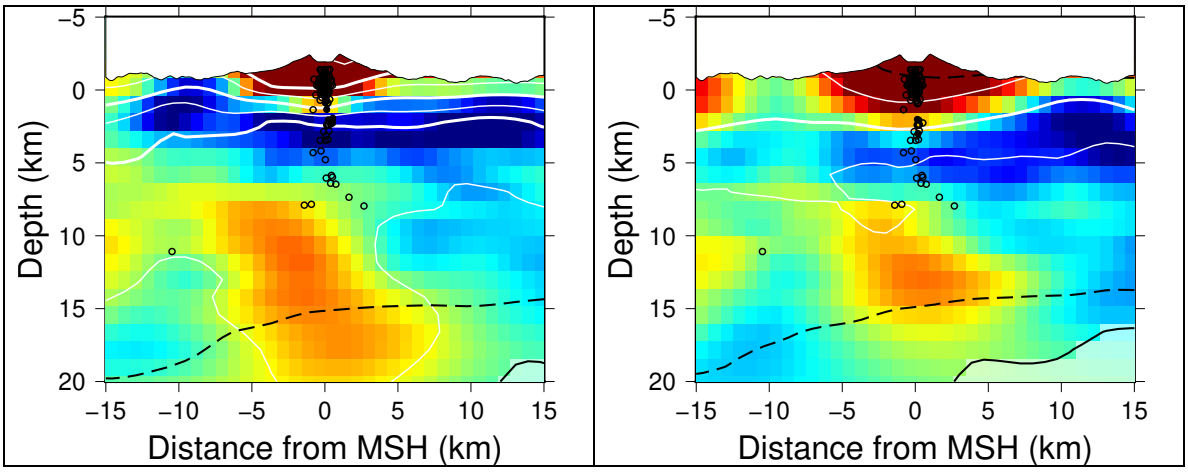

Figure 3.5. *Vp* and *Vs* model cross-sections at MSH.

W-E cross-sections through MSH for the *Vp* (left) and *Vs* (right) models. Contours and earthquakes same as Figure 2.

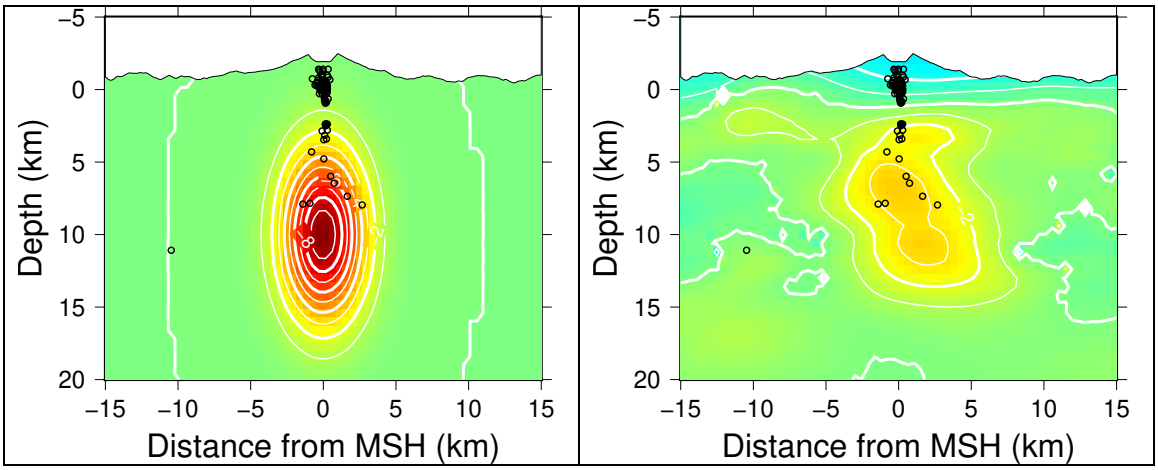

Figure 3.6. Resolution testing for MSH magma feature.

Resolution testing for a potential magma storage region beneath MSH. From an input anomaly (left) with 4-km diameter and 10% negative *Vp* perturbation we recover an anomaly (right) with 6-7 km diameter and 3.5-4% negative perturbation.

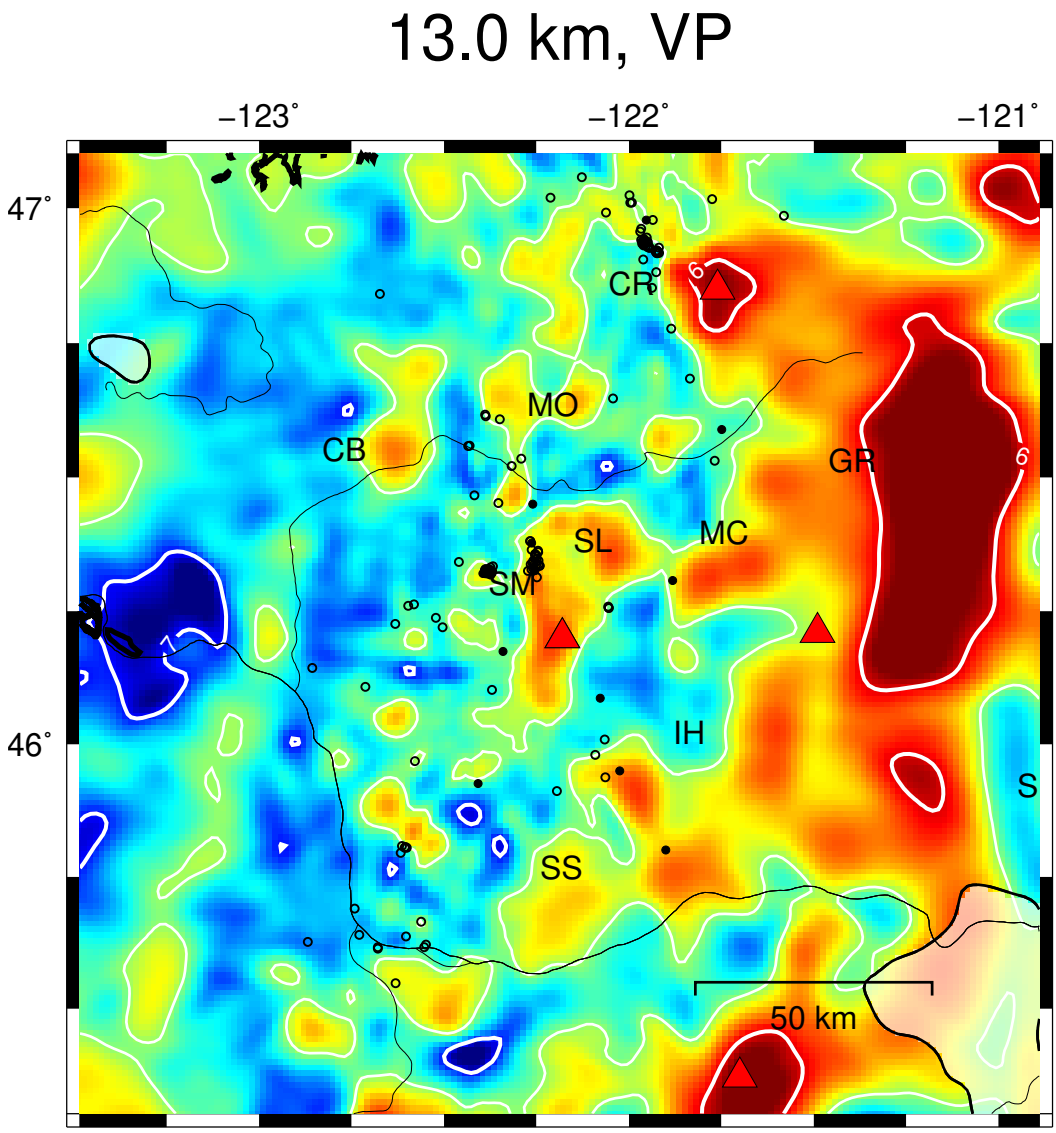

Figure 3.7. Large *Vp* model depth slice at 13 km.

Depth slice through larger *Vp* model at 13 km below sea level, showing percent variation from a 1-D model. Contours and earthquakes same as Figure 1, except semblance contour (black dashed line) is for features with wavelength of 40-km instead of 20-km. Red triangles indicate position of MSH and Mount Adams, letter codes are the same as in Figure 1B.

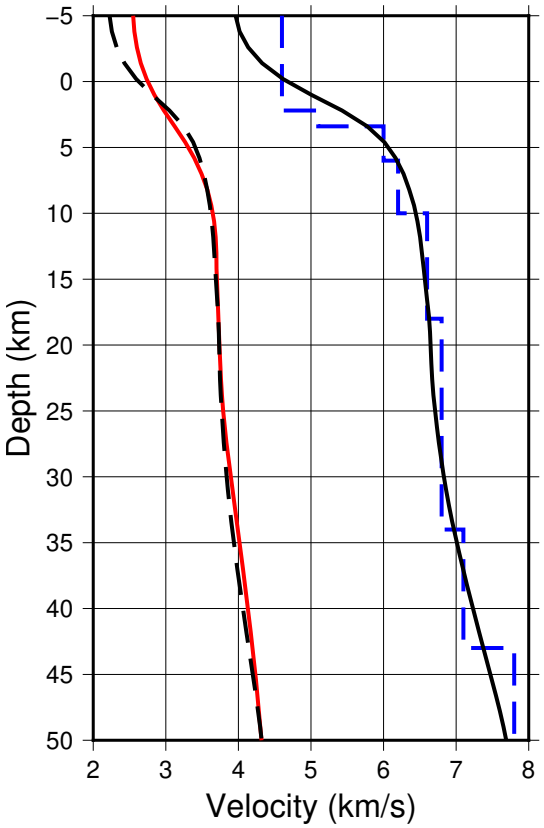

Figure 3.8. 1-D seismic velocity profiles.

Seismic velocity profiles for the models discussed, including the average within 50 km of MSH for the *Vp* model (solid black) and the *Vs* model (solid red), as well as the PNSN S4 model for MSH (dashed blue), and the average *Vp* model divided by 1.78 (dashed black).

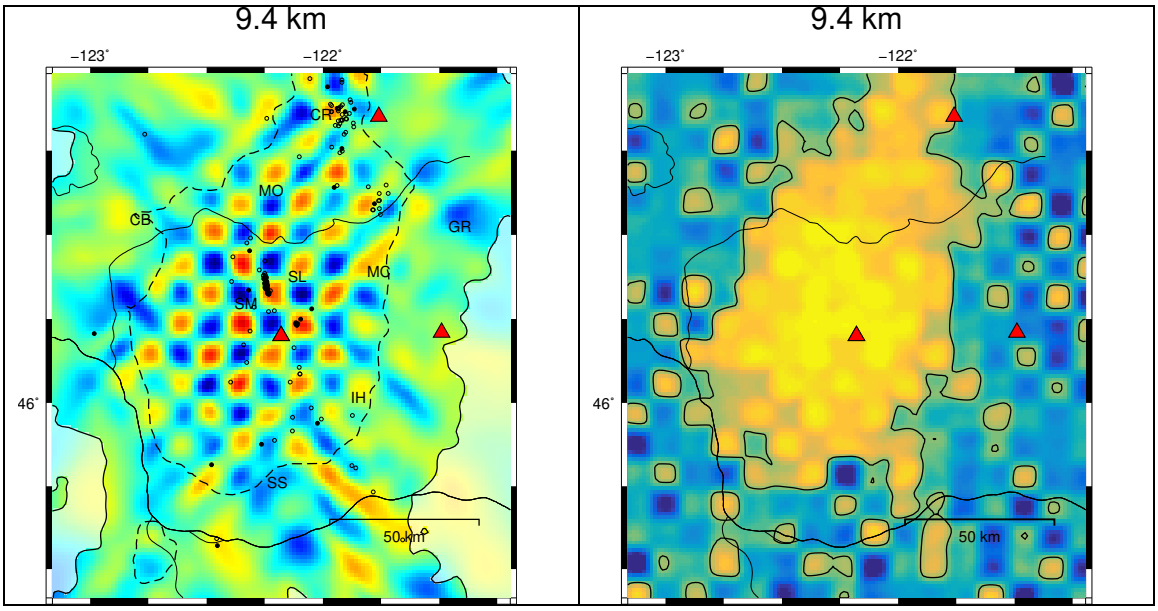

Figure 3.S1. Example checkerboard and semblance test for *Vp* at 9.4 km.

Example checkerboard resolution test (left), and resulting semblance values for one checkerboard (right), for the *Vp* model at 9.4 km depth. In the semblance plot the black contour is for a semblance value of 0.7. To obtain the semblance values used in the analysis, we use 16 different checkerboards, as described in the text.

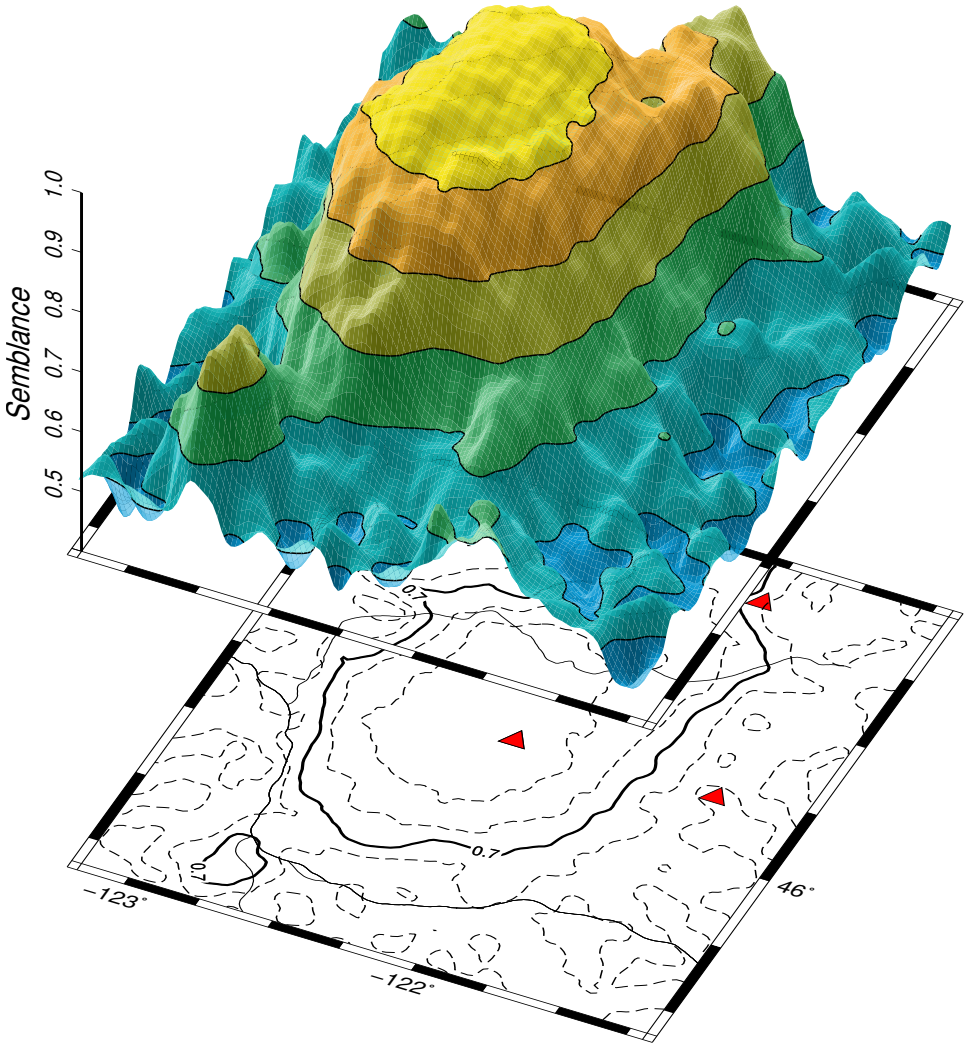

Figure 3.S2. Full 10-km feature semblance for *Vp* at 9.4 km depth.

A 3d view of the semblance surface for the *Vp* model at 9.4 km depth, with contours (black lines) every 0.1 units, to indicate the relatively abrupt change from resolved to not-resolved.

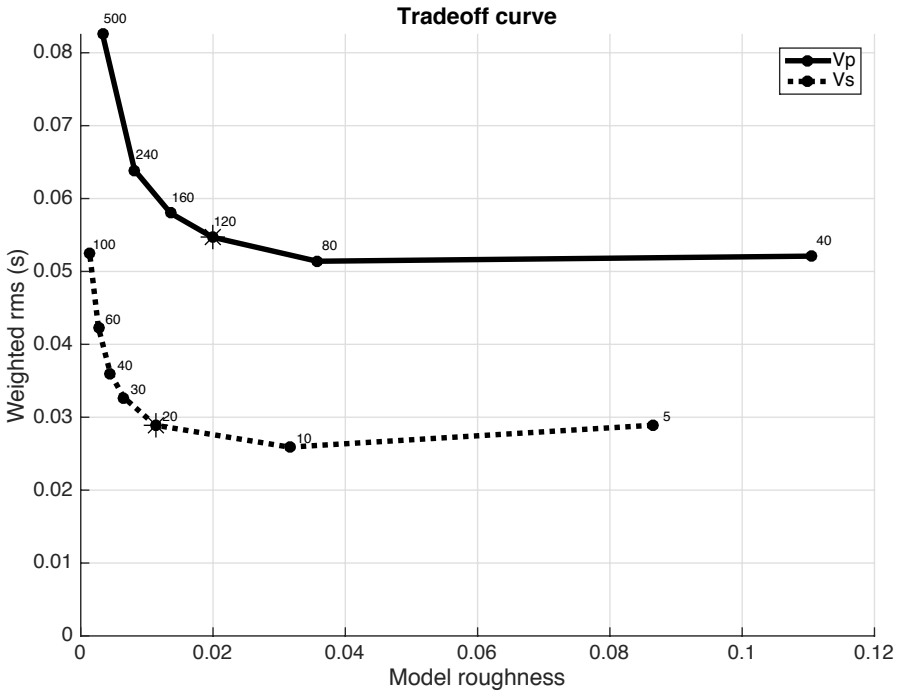

Figure 3.S3. Tradeoff curve.

Tradeoff curve for the *Vp* and *Vs* inversions, showing the model roughness and weighted rms misfit for different tradeoff parameters. The models shown are marked with an asterisk.

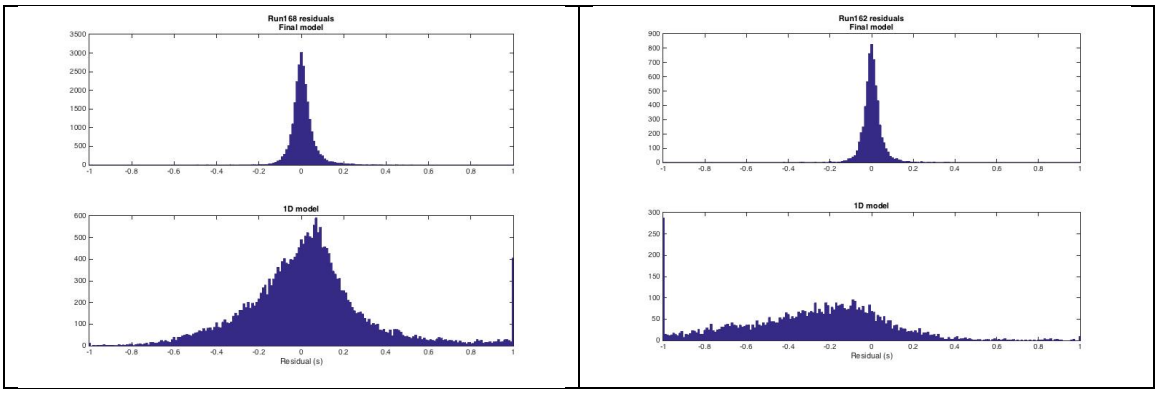

Figure 3.S4. Travel-time residual from 1-D and 3-D models.

Travel-time residual reduction from the 1d input model (bottom) to the 3d final model (top) for the *Vp* (left) and *Vs* models (right)

Data source	# Stations	Dates	# Sources	# Picks	Reference
iMUSH broadband	70	June 2014-Aug 2016	399 earthquakes	10511 *P* 5627 *S*	This paper
		July-Aug 2014	23 shots	1309 *P*	Kiser et al., 2016
iMUSH Nodal	719	July-Aug 2014	8 earthquakes	1876 *P*	Hansen and Schmandt, 2015
Parsons active line	963	1995	8 shots	3626 *P*	Parsons et al., 1998
AltaRock broadband	20	June-Nov 2016	46 earthquakes	639 *P* 432 *S*	YH - 2016
PNSN iMUSH supplement	95	June 2014-Aug 2016	63 earthquakes	920 *P* 41 *S*	This paper
PNSN catalog since 2009	133	Jan 2009-Aug 2016	205	6344	See Data and Resources
Total	**1905 unique stations**		**640 unique sources**	**25225 *P*** **6100 *S***	

Table 3.1. Data sources used in velocity model inversions.

Feature	***Vp* anomaly**	***Vp* max**	***Vs* anomaly**	***Vs* max**	**Depth**	**Apx max dim.**	**Apx max volume**	**Ratio**
Unit	**%**	**km/s**	**%**	**km/s**	**km**	**km**	**km^3**	***Vp*/*Vs***
SM	+23	6.22	+24, +21	3.62, 3.53	s-4	10x20	800	1.71
SL	+21	6.12	+14	3.33	s-4	15x20	1200	1.76
MC	+21	6.12	+20	3.50	s-4	10x20	800	1.84
SS	+27	6.42	+30	3.80	s-4	15x20	1200	1.75
-35, -10	+14	5.77	+21	3.53	s-4	10x5	200	1.69
-12, -20	+16	5.87	+8	3.15	s-3	5x10	150	1.63
2, -10	+19	6.02	-10	2.63	s-3	5x8	120	2.29
32, 32	+12	5.66	+5	3.07	s-3	10x5	150	1.85
TA	+20	6.07	-	-	s-4	~30x25	3000	-
IH	-16	4.25	-20	2.34	s-3	15x20	900	1.82
CB	-30	3.54	-27	2.13	s-7	40x50	14000	1.66
MO	-19	4.10	-11	2.60	s-7	5x10	350	1.58
Arc	-12	5.47-5.68	-	-	7-16	~40x80	28800	-
SL	-6	5.85-6.19	-5	3.41-3.60	7-16	15x15	2025	1.72
MC	-8	5.29-5.86	-6	3.13-3.46	3-10	15x30	3150	1.69
20,40 (SK)	-8	5.29-5.94	-4	3.20-3.58	3-12	10x10	900	1.66
SHZ	-5	4.75-6.25	-5	2.76-3.59	s-16	5x40	3200	1.73
SS	-6	5.90-6.19	-10	3.27-3.41	8-16	10x15	1200	1.81
MR	-10	5.40-5.92	-	-	5-16	10x20	2200	-
MSH	-5	5.81-6.23	-5	3.36-3.59	6-15	6x6	324	1.73

Table 3.2. Description of velocity anomalies for 3-D *Vp* and *Vs* models.

Italics- surface anomaly; **Bold**- mid-crustal anomaly; s=surface; SM=Spud Mountain pluton; SL=Spirit Lake pluton; MC=McCoy Creek quartz diorite; SS=Silver Star pluton; TA=Tatoosh pluton; IH=Indian Heaven volcanic field; CB=Chehalis basin; MO=Morton anticline; Arc=Mount Adams to Goat Rocks to Mount Rainier; SK=Skate Mountain anticline; SHZ=Mount St. Helens seismic zone; MR=Mount Rainier.
Numbers in first column are east, north coordinates (km) relative to MSH.
(Apx max volume) = (depth range) * (max area)

Input diameter (km)	Input perturbation (-%)	Output perturbation (-%)	Output diameter (km)	Best depth range (km b.s.l.)
2	10	1 - 2.5	5-10	5-10
2	20	1 - 3	5	5-8
4	10	3.5 - 4	6-7	5-12
4	20	4 - 8	6-9	5-8
8	10	7 - 8	7-10	2-15
8	20	12 - 16	9-10	2-15

Table 3.3. Resolution of shallow magma storage region beneath MSH.

Site	Latitude	Longitude	Elevation (m)	Percent data recovered
MA05	46.75467	-122.22619	488	91.3
MB05	46.62087	-122.28102	641	98.1
MB07	46.62378	-122.04239	878	100.0
MC06	46.55202	-122.1572	770	98.1
MC08	46.55335	-121.96322	653	100.0
MD05	46.52316	-122.27817	718	100.0
MD09	46.50288	-121.70671	959	96.3
MD12	46.47694	-121.22067	1496	95.0
ME02	46.43916	-122.70734	158	100.0
ME03	46.45207	-122.57647	310	92.5
ME04	46.45061	-122.35194	730	85.0
ME06	46.46329	-122.19697	643	98.0
ME08	46.46195	-121.86564	598	90.0
MF05	46.39037	-122.38676	727	87.5
MF07	46.42563	-122.00227	515	80.6
MF09	46.38994	-121.861	1216	100.0
MG02	46.37375	-122.73487	162	87.5
MG03	46.33807	-122.47619	638	100.0
MG05	46.30588	-122.34193	1283	100.0
MG06	46.35014	-122.21745	1408	98.1
MG07	46.35285	-122.03101	1457	100.0
MG08	46.34174	-121.92873	1547	100.0
MG10	46.34472	-121.65809	893	100.0
MH01	46.2639	-122.80627	197	100.0
MH03	46.26842	-122.59412	373	100.0
MH04	46.27946	-122.42707	920	100.0
MH07	46.27981	-122.08202	1122	81.3
MH09	46.29767	-121.80103	989	96.3
MH11	46.27071	-121.57848	1447	100.0
MI02	46.21624	-122.66592	349	81.3
MI04	46.19594	-122.41015	918	100.0
MI05	46.2311	-122.29212	1255	100.0
MI07	46.24823	-122.07328	1124	98.8
MI08	46.25385	-121.97448	1246	86.3
MI09	46.22937	-121.83447	1003	100.0
MI10	46.21928	-121.67823	1001	100.0
MJ01	46.19374	-122.81126	339	100.0

MJ02	46.13877	-122.7012	317	98.1
MJ03	46.1591	-122.56496	397	97.5
MJ06	46.16705	-122.26062	976	95.0
MJ07	46.17878	-122.05578	509	77.5
MJ09	46.18418	-121.92144	1052	87.5
MK04	46.1127	-122.39086	482	98.8
MK06	46.11837	-122.19218	680	87.5
MK07	46.1527	-122.11677	929	100.0
MK08	46.11738	-122.04607	762	98.8
MK10	46.14467	-121.77133	1186	100.0
MK11	46.15254	-121.60194	1343	100.0
MK12	46.1137	-121.36388	1226	50.0
ML03	46.06243	-122.51601	356	100.0
ML07	46.07427	-122.11523	694	98.8
ML09	46.07809	-121.88036	1144	100.0
ML10	46.05278	-121.75087	1238	100.0
ML11	46.0756	-121.61633	1033	100.0
MM02	46.01971	-122.68467	209	100.0
MM04	46.01525	-122.34545	313	99.4
MM06	46.04118	-122.25688	601	97.5
MM08	46.03273	-121.98412	1019	92.5
MN07	45.99261	-122.08166	861	100.0
MN09	46.00074	-121.8419	1254	72.5
MN10	45.98163	-121.68044	1091	100.0
MO03	45.92685	-122.57483	254	77.5
MO06	45.93212	-122.20608	784	100.0
MO07	45.88513	-122.08445	1248	95.0
MP03	45.82557	-122.4944	126	68.1
MP04	45.81266	-122.38093	497	71.9
MP06	45.83138	-122.19591	796	91.3
MP08	45.86615	-121.91156	781	65.0
MP10	45.89865	-121.80077	1130	100.0
MQ07	45.80818	-122.10721	1037	88.8

Table 3.S1. Station location and data recovery.

IV. Earthquake relocation in the Mount St. Helens region

4.1. Introduction

We have relocated ~26000 Pacific Northwest Seismic Network (PNSN) catalog earthquakes in the Mount St. Helens (MSH) area, going back to 1980. We use the best-fit 3-D *Vp* and *Vs* models from the local earthquake tomography performed in Chapter 3 in order to do this.

4.2. Methods

We generate travel-time grids for each station within the velocity model area that had a PNSN catalog travel time pick for any of the events of interest. These grids are produced using the forward-modeling portion of the struct3dp program used in the velocity inversion. The first-arrival travel time between each grid node and a given station is calculated using a finite-difference 3-D eikonal equation solver (Vidale, 1990; Hole and Zelt, 1995).

Then for each event we perform a grid search over the model area within 10 km of the PNSN catalog location and define the hypocenter misfit using an L2-norm at a given node *k* as:

$$M_k = \sum_{i=1}^{n} \frac{\left(t_{obs_{ik}} - t_{or_k} - tt_{ik}\right)^2}{\sigma_i^2} \quad (1)$$

where M_k is the misfit, $t_{obs_{ik}}$ is the observed arrival time at station *i* for node *k*, t_{or_k} is the hypocenter origin time, tt_{ik} is the travel time from station *i* to grid node *k*, *n* is the number of observed arrival times for the given event, and σ_i is the arrival time uncertainty. To find the best-fitting origin time for an earthquake at this location, we set the derivative of the misfit with respect to t_{or_k} , $\frac{dM_k}{dt_{or_k}}$, equal to zero. After simplification, we obtain

$$t_{or_k} = \frac{\sum_{i=1}^{n} [(t_{obs_{ik}} - tt_{ik})/\sigma_i^2]}{\sum_{i=1}^{n} [1/\sigma_i^2]} \quad (2)$$

Using t_{or_k}, we can calculate the misfit, M_k, at this grid node. After performing this process at each grid node, we find the minimum misfit value to obtain the best-fitting hypocenter for the given event. To improve the location, we repeat the process near the initial location over a finer interpolated grid, with side length equal to 60m. In all cases, we restrict the grid search to be below local land elevation, so that there will not be any "airquakes."

In addition to a location determined using an L2-norm misfit, we find another location that minimizes an L1-norm misfit. This is done in order to minimize and evaluate the effect of outliers on the relocation. The L1-norm misfit at a given node *k* is:

$$M_k = \sum_{i=1}^{n} \frac{\left| t_{obs_{ik}} - t_{or_k} - tt_{ik} \right|}{\sigma_i} \tag{3}$$

where the | | symbols represent the absolute value, and the variables are the same as in equation 1. Since t_{or_k} cannot be calculated analytically as for the L2-norm function, an additional grid search is performed over origin time as well as space in order to find the hypocenter which minimizes the misfit function. Again, the process is repeated over a finer interpolated grid with side-length 60m to find the best-fitting hypocenter.

We calculate location uncertainty by assuming the L2-norm misfit function follows a chi-squared distribution, and find the distance in the *x*, *y*, and *z* directions to the misfit value that would explain 95% of the data variation. To account for outliers we scale the misfit function so that the minimum value corresponds to the expected value of the chi-squared distribution with *n*-4 degrees of freedom (where 4 represents the four hypocentral parameters).

4.3. Results

We relocated 26000 earthquakes within 100 km of MSH. On average, the distance moved is less than 1.5 km, although there are ~2000 events which are relocated more than 3 km from the original PNSN catalog location. The median 95%-confidence horizontal and vertical location errors for the relocated earthquakes using the L2-norm method are 0.75 km and 1.2 km, respectively.

The median root-mean-square (RMS) residual of the PNSN locations for earthquakes within 1km of MSH is 0.114s (for a 1-D velocity model including station corrections), while the median RMS residual of the relocated earthquakes near MSH through the 3-D models is 0.159s using the L2-norm method and 0.167s using the L1-norm method. For earthquakes more than 1km from MSH, the median RMS residual for the original locations through a 1-D model is 0.203s, while the L2-norm RMS residual is 0.173s and the L1-norm RMS residual is 0.180s. We believe the lower RMS residual for the PNSN locations near MSH is related to the station corrections used with the 1-D model. About half of the earthquakes relocated between 1980 and 2018 were within 5km of MSH.

4.4. Supplementary Material

The catalog of relocated earthquakes is provided as a text file. Each line describes a single earthquake with the following fields:

orid – PNSN origin id
mag – PNSN-derived magnitude
yy – PNSN origin time, year
mm – PNSN origin time, month
dd – PNSN origin time, day
HH – PNSN origin time, hour
MM – PNSN origin time, minutes
SS.fff – PNSN origin time, seconds

latPNSN – PNSN location, latitude
lonPNSN – PNSN location, longitude
depPNSN – PNSN location, depth below sea level (km)
latL2 – L2 method location, latitude
lonL2 – L2 method location, longitude
depL2 – L2 method location, depth below sea level (km)
tL2-tPNSN – time difference between L2 and PNSN hypocenters (s)
latL1 – L1 method location, latitude
lonL1 – L1 method location, longitude
depL1 – L1 method location, depth below sea level (km)
tL1-tPNSN – time difference between L1 and PNSN hypocenters (s)
npPNSN – number of *P* phases used in PNSN 1-D location
nsPNSN – number of *S* phases used in PNSN 1-D location
npReloc – number of *P* phases used in L2 and L1 relocations
nsReloc – number of *S* phases used in L2 and L1 relocations
azPNSN – greatest azimuthal gap between stations for PNSN location (degrees)
azReloc – greatest azimuthal gap between stations for L2 and L1 relocations (degrees)
cloPNSN – closest station used in PNSN location (km)
cloReloc – closest station used in L2 and L1 relocations (km)
rmsPNSN – RMS residual through 1-D velocity model for PNSN location (s)
rmsL2 – RMS residual through 3-D velocity model for L2 relocation (s)
rmsL1 – RMS residual through 3-D velocity model for L1 relocation (s)
xerrL2 – 95% location error for L2 relocation in E-W direction (km)
yerrL2 – 95% location error for L2 relocation in N-S direction (km)
zerrL2 – 95% location error for L2 relocation in vertical direction (km)

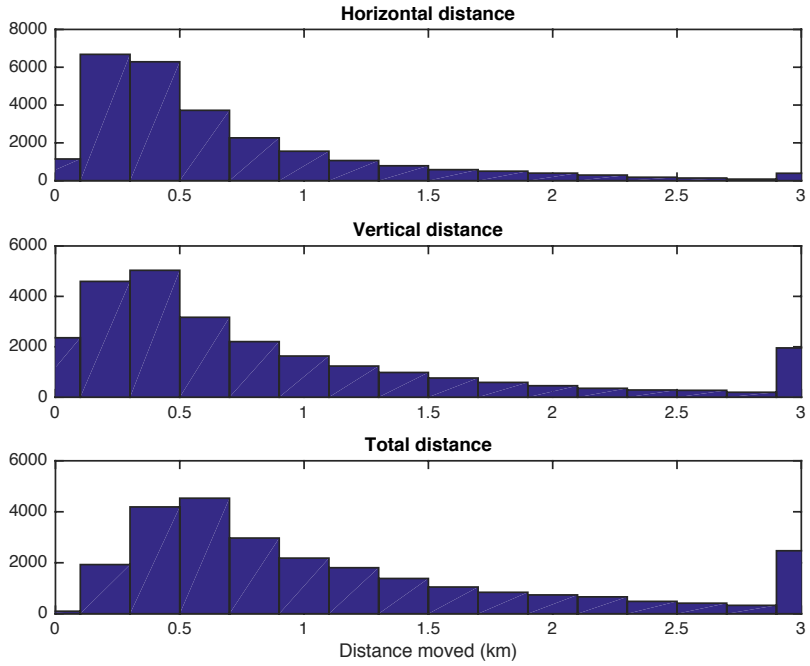

Figure 4.1. Relocation distance.

Horizontal (top), vertical (middle), and total (bottom) distance between relocated earthquakes and original PNSN location.

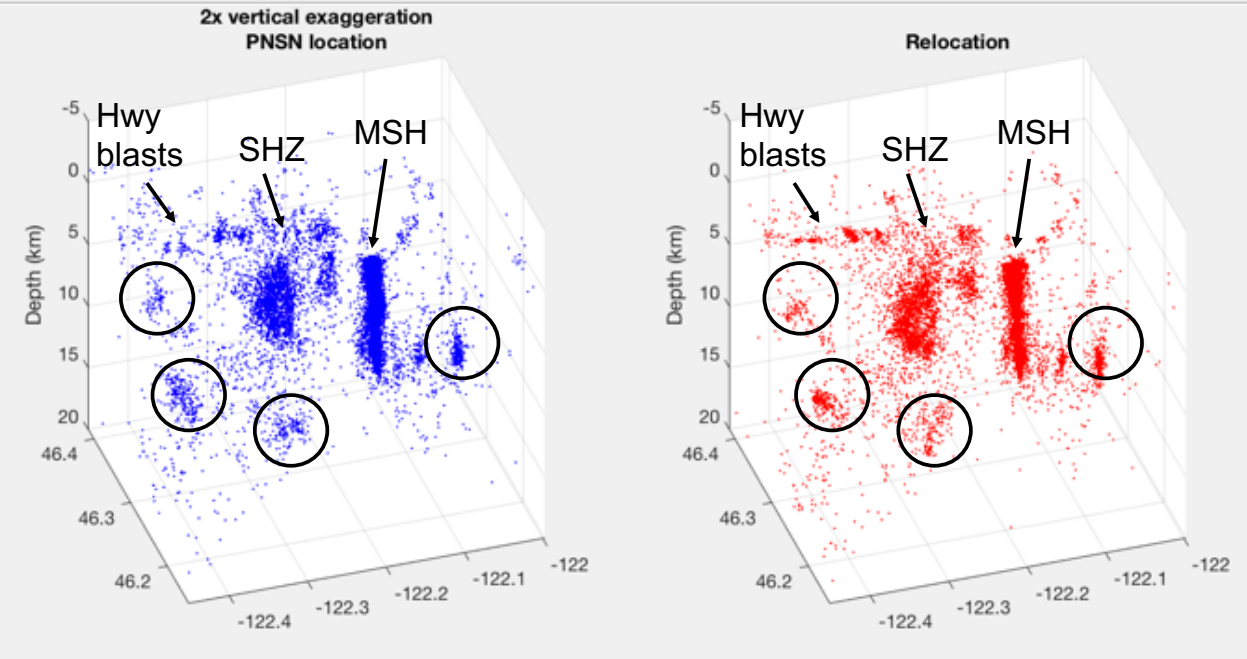

Figure 4.2. Original vs. relocated locations, map.

Relocated events (right) show tighter clustering in certain areas (circled), including along the Mount St. Helens seismic zone (SHZ) and beneath MSH itself.

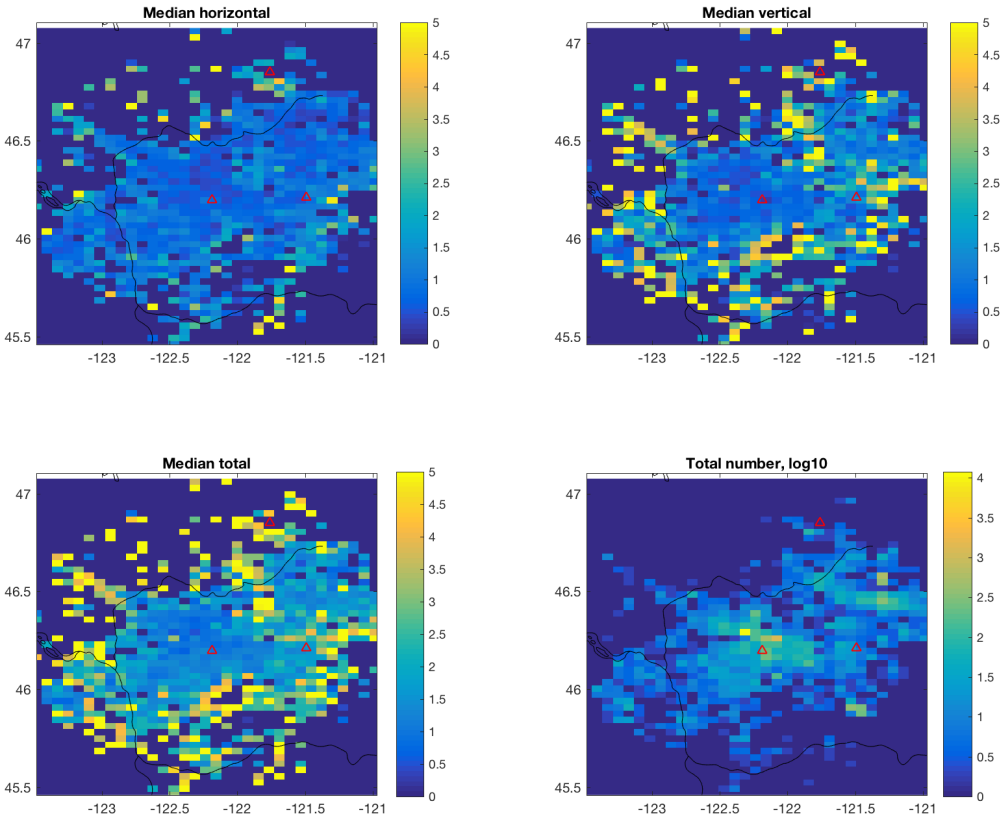

Figure 4.3. Map view of median relocation distance.

Median horizontal, vertical, and total distance, plus number of events in each .05 x .05 degree map area.

V. Summary

5.1. Tremor source amplitudes in northern Cascadia

The northern Cascadia ETS events from 2007-2010 exhibited similar spatiotemporal patterns of radiated energy from tectonic tremor. In the initiation phase of each event, during which tremor started downdip and moved updip over ~8 days, the tremor area and tremor amplitudes increased quasi-linearly, implying a constant radiated energy rate per unit area and a diffusional process for tremor migration. During this time, the tremor amplitudes did not exhibit a strong sensitivity to tidal stress fluctuations. Once the tremor filled the downdip width of the tremoring region, the ETS events began to propagate to the north and south at a constant rate, with the amplitudes being strongly modulated by tidal stresses. This implies a generally low effective normal stress or low effective friction along the plate interface, which begins higher during the initiation of an ETS event and decreases as the ETS grows to the point where small tidal stress fluctuations can modulate the energy released during slow slip.

5.2. Tectonic history and magmatic structure of the Mount St. Helens region using local earthquake *Vp* and *Vs* tomography

I calculate 3-D *Vp* and *Vs* models and provide supporting evidence for several broad interpretations of the geologic setting and tectonic history of the Mount St. Helens (MSH) area. The largest anomalies in the seismic velocity models occur near the surface, and correlate very closely with geological features mapped at the surface, including many Miocene-aged plutons, Quaternary-aged and Tertiary-aged sedimentary basins and units, and the Indian Heaven volcanic field. At depths of 5-15 km, we see low *Vp* and *Vs* along the Mount St. Helens seismic zone, which corresponds very closely with high conductive anomalies, indicating the possible

presence of fluids and sedimentary rocks from the accretion of the Siletz terrane. This correspondence between low velocities and high conductivities continues towards the east, essentially framing the edge of the previously imaged Southwest Washington Cascades Conductor (SWCC). Beneath MSH, we image low *P*- and *S*-wave velocities at 6-15 km depth, in a roughly cylindrical shape, which could indicate the presence of a narrower zone of partial melt storage beneath the volcano, possibly holding up to 5-10 km^3 of partial melt. Finally, we image a large, low *Vp* region at depths of 10-20 km in the mid-crust beneath and to the east of Mount Adams and stretching towards Mount Rainier. This area is likely host to higher temperatures and some amount of partial melt associated with the primary magmatic axis in this region of the Cascades.

These results will be further compared and in some cases inverted with other portions of the iMUSH project. I intend to use the active-source data set from Kiser et al. (2018) in cooperation with Kiser to perform a larger inversion of both data sets. This will provide further constraints on the velocity models, especially at shallow depths, since the active source station spacing was in some cases as low as 100 meters.

Reference list

Aguiar, A. C., T. I. Melbourne, and C. W. Scrivner (2009), Moment release rate of Cascadia tremor constrained by GPS, *Journal of Geophysical Research-Solid Earth, 114*, B00A05, doi: 10.1029/2008JB005909.

Aso, N., K. Ohta, and S. Ide (2013), Tectonic, volcanic, and semi-volcanic deep low-frequency earthquakes in western Japan, *Tectonophysics, 600*, 27-40, doi: 10.1016/j.tecto.2012.12.015.

Atwater, B. (1987), Evidence for great Holocene earthquakes along the outer coast of Washington State, *Science, 236*(4804), 942-944, doi: 10.1126/science.236.4804.942.

Baltay, A. S. and G. C. Beroza (2013), Ground-motion prediction from tremor, *Geophys. Res. Lett., 40*(24), 6340-6345, doi: 10.1002/2013GL058506.

Barker, S. and S. Malone (1991), Magmatic system geometry at Mount St. Helens modeled from the stress-field associated with posteruptive earthquakes, *Journal of Geophysical Research-Solid Earth and Planets, 96*(B7), 11883-11894, doi: 10.1029/91JB00430.

Bedrosian, P. A. and D. W. Feucht (2014), Structure and tectonics of the northwestern United States from Earth Scope USArray magnetotelluric data, *Earth Planet. Sci. Lett., 402*, 275-289, doi: 10.1016/j.epsl.2013.07.035.

Bedrosian, P. A., J. R. Peacock, E. Bowles-Martinez, A. Schultz, and G. J. Hill (2018), Crustal inheritance and a top-down control on arc magmatism at Mount St. Helens, *Nature Geoscience, in press*.

Blackwell, D., J. Steele, S. Kelley, and M. Korosec (1990), Heat-flow in the state of Washington and thermal conditions in the Cascade Range, *Journal of Geophysical Research-Solid Earth and Planets, 95*(B12), 19495-19516, doi: 10.1029/JB095iB12p19495.

Blakely, R., T. Brocher, and R. Wells (2005), Subduction-zone magnetic anomalies and implications for hydrated forearc mantle, *Geology, 33*(6), 445-448, doi: 10.1130/G21447.1.

Bostock, M. G., A. M. Thomas, G. Savard, L. Chuang, and A. M. Rubin (2015), Magnitudes and moment-duration scaling of low-frequency earthquakes beneath southern Vancouver Island, *Journal of Geophysical Research-Solid Earth, 120*(9), 6329-6350, doi: 10.1002/2015JB012195.

Brocher, T. M., R. E. Wells, A. P. Lamb, and C. S. Weaver (2017), Evidence for distributed clockwise rotation of the crust in the northwestern United States from fault geometries and focal mechanisms, *Tectonics, 36*(5), 787-818, doi: 10.1002/2016TC004223.

Brudzinski, M. R. and R. M. Allen (2007), Segmentation in episodic tremor and slip all along Cascadia, *Geology, 35*(10), 907-910, doi: 10.1130/G23740A.1.

Chestler, S. R. and K. C. Creager (2017), Evidence for a scale-limited low-frequency earthquake source process, *Journal of Geophysical Research-Solid Earth, 122*(4), 3099-3114, doi: 10.1002/2016JB013717.

Christensen, N. (1979), Compressional wave velocities in rocks at high-temperatures and pressures, critical thermal-gradients, and crustal low-velocity zones, *Journal of Geophysical Research, 84*(NB12), 6849-6857, doi: 10.1029/JB084iB12p06849.

Christensen, N. and W. Mooney (1995), Seismic velocity structure and composition of the continental crust - a global view, *Journal of Geophysical Research-Solid Earth, 100*(B6), 9761-9788, doi: 10.1029/95JB00259.

De Siena, L., M. Calvet, K. J. Watson, A. R. T. Jonkers, and C. Thomas (2016), Seismic scattering and absorption mapping of debris flows, feeding paths, and tectonic units at Mount St. Helens volcano, *Earth Planet. Sci. Lett., 442*, 21-31, doi: 10.1016/j.epsl.2016.02.026.

Duncan, R. (1982), A captured island chain in the Coast Range of Oregon and Washington, *Journal of Geophysical Research, 87*(NB13), 827-837, doi: 10.1029/JB087iB13p10827.

Egbert, G. and J. Booker (1993), Imaging crustal structure in southwestern Washington with small magnetometer arrays, *Journal of Geophysical Research-Solid Earth, 98*(B9), 15967-15985, doi: 10.1029/93JB00778.

Evarts, R., R. Ashley, and J. Smith (1987), Geology of the Mount St. Helens area - Record of discontinuous volcanic and plutonic activity in the Cascade arc of southern Washington, *Journal of Geophysical Research-Solid Earth and Planets, 92*(B10), 10155-10169, doi: 10.1029/JB092iB10p10155.

Finn, C. (1990), Geophysical constraints on Washington convergent margin structure, *Journal of Geophysical Research-Solid Earth and Planets, 95*(B12), 19533-19546, doi: 10.1029/JB095iB12p19533.

Finn, C. and D. Williams (1987), An aeromagnetic study of Mount St. Helens, *Journal of Geophysical Research-Solid Earth and Planets, 92*(B10), 10194-10206, doi: 10.1029/JB092iB10p10194.

Flinders, A. F. and Y. Shen (2017), Seismic evidence for a possible deep crustal hot zone beneath Southwest Washington, *Scientific Reports, 7*, 7400, doi: 10.1038/s41598-017-07123-w.

Ghosh, A., J. E. Vidale, and K. C. Creager (2012), Tremor asperities in the transition zone control evolution of slow earthquakes, *Journal of Geophysical Research-Solid Earth, 117*, B10301, doi: 10.1029/2012JB009249.

Hagstrum, J., D. Swanson, and L. Snee (1998), Paleomagnetism of the Miocene intrusive suite of Kidd Creek: Timing of deformation in the Cascade arc, southern Washington, *Journal of Geophysical Research-Solid Earth, 103*(B9), 21047-21056, doi: 10.1029/98JB02051.

Hansen, S. M., B. Schmandt, A. Levander, E. Kiser, J. E. Vidale, G. A. Abers, and K. C. Creager (2016), Seismic evidence for a cold serpentinized mantle wedge beneath Mount St. Helens, *Nature Communications, 7*, 13242, doi: 10.1038/ncomms13242.

Hansen, S. M. and B. Schmandt (2015), Automated detection and location of microseismicity at Mount St. Helens with a large-N geophone array, *Geophys. Res. Lett., 42*(18), 7390-7397, doi: 10.1002/2015GL064848.

Hawthorne, J. C. and A. M. Rubin (2010), Tidal modulation of slow slip in Cascadia, *Journal of Geophysical Research-Solid Earth, 115*, B09406, doi: 10.1029/2010JB007502.

Heliker, C. (1995), Inclusions in Mount St. Helens dacite erupted from 1980 through 1983, *J. Volcanol. Geotherm. Res., 66*(1-4), 115-135, doi: 10.1016/0377-0273(94)00074-Q.

Hildreth, W. (2007), Quaternary magmatism in the Cascades- Geologic perspectives, *U. S. Geol. Surv. Prof. Pap., 1744*.

Hill, G. J., T. G. Caldwell, W. Heise, D. G. Chertkoff, H. M. Bibby, M. K. Burgess, J. P. Cull, and R. A. F. Cas (2009), Distribution of melt beneath Mount St Helens and Mount Adams inferred from magnetotelluric data, *Nature Geoscience, 2*(11), 785-789, doi: 10.1038/NGEO661.

Hoblitt, R., D. Crandell, and D. Mullineaux (1980), Mount St. Helens eruptive behavior during the past 1,500 Yr, *Geology, 8*(11), 555-559, doi: 10.1130/0091-7613(1980)8<555:MSHEBD>2.0.CO;2.

Hole, J. and B. Zelt (1995), 3-D finite-difference reflection travel-times, *Geophysical Journal International, 121*(2), 427-434, doi: 10.1111/j.1365-246X.1995.tb05723.x.

Houston, H. (2015), Low friction and fault weakening revealed by rising sensitivity of tremor to tidal stress, *Nature Geoscience, 8*(5), 409-+, doi: 10.1038/NGEO2419.

Houston, H., B. G. Delbridge, A. G. Wech, and K. C. Creager (2011), Rapid tremor reversals in Cascadia generated by a weakened plate interface, *Nature Geoscience, 4*(6), 404-409, doi: 10.1038/NGEO1157.

Ide, S. (2010), Striations, duration, migration and tidal response in deep tremor, *Nature, 466*(7304), 356-U105, doi: 10.1038/nature09251.

Kirby, S. H., K. Wang, and T. M. Brocher (2014), A large mantle water source for the northern San Andreas fault system: a ghost of subduction past, *Earth Planets and Space, 66*, 67, doi: 10.1186/1880-5981-66-67.

Kiser, E., A. Levander, C. Zelt, B. Schmandt, and S. Hansen (2018), Focusing of melt near the top of the Mount St. Helens (USA) magma reservoir and its relationship to major volcanic eruptions, *Geology, submitted*.

Kiser, E., I. Palomeras, A. Levander, C. Zelt, S. Harder, B. Schmandt, S. Hansen, K. Creager, and C. Ulberg (2016), Magma reservoirs from the upper crust to the Moho inferred from high-resolution Vp and Vs models beneath Mount St. Helens, Washington State, USA, *Geology, 44*(6), 411-414, doi: 10.1130/G37591.1.

Leaver, D., W. Mooney, and W. Kohler (1984), A seismic refraction study of the Oregon Cascades, *Journal of Geophysical Research, 89*(NB5), 3121-3134, doi: 10.1029/JB089iB05p03121.

Lees, J. (1992), The magma system of Mount St. Helens - Nonlinear high-resolution P-wave tomography, *J. Volcanol. Geotherm. Res., 53*(1-4), 103-116, doi: 10.1016/0377-0273(92)90077-Q.

Lees, J. and R. Crosson (1989), Tomographic inversion for 3-dimensional velocity structure at Mount St. Helens using earthquake data, *Journal of Geophysical Research-Solid Earth and Planets, 94*(B5), 5716-5728, doi: 10.1029/JB094iB05p05716.

Maeda, T. and K. Obara (2009), Spatiotemporal distribution of seismic energy radiation from low-frequency tremor in western Shikoku, Japan, *Journal of Geophysical Research-Solid Earth, 114*, B00A09, doi: 10.1029/2008JB006043.

Malone, S. D. and G. L. Pavlis (1983), Velocity structure and relocation of earthquakes at Mount St. Helens (abstract), *EOS Trans. AGU, 64*, Fall Meet. Suppl., 895.

Mattinson, J. M. (1977), Emplacement history of the Tatoosh volcanic-plutonic complex, Washington: Ages of zircons, *GSA Bulletin, 88*, 1509--1514.

McCaffrey, R., R. W. King, S. J. Payne, and M. Lancaster (2013), Active tectonics of northwestern U. S. inferred from GPS-derived surface velocities, *Journal of Geophysical Research-Solid Earth, 118*(2), 709-723, doi: 10.1029/2012JB009473.

McCrory, P. A., J. L. Blair, F. Waldhauser, and D. H. Oppenheimer (2012), Juan de Fuca slab geometry and its relation to Wadati-Benioff zone seismicity, *Journal of Geophysical Research-Solid Earth, 117*, B09306, doi: 10.1029/2012JB009407.

Meqbel, N. M., G. D. Egbert, P. E. Wannamaker, A. Kelbert, and A. Schultz (2014), Deep electrical resistivity structure of the northwestern US derived from 3-D inversion of USArray magnetotelluric data, *Earth Planet. Sci. Lett., 402*, 290-304, doi: 10.1016/j.epsl.2013.12.026.

Miller, R. (1989), The Mesozoic Rimrock Lake inlier, southern Washington Cascades - Implications for the basement to the Columbia Embayment, *Geological Society of America Bulletin, 101*(10), 1289-1305, doi: 10.1130/0016-7606(1989)101<1289:TMRLIS>2.3.CO;2.

Moran, S., J. Lees, and S. Malone (1999), P wave crustal velocity structure in the greater Mount Rainier area from local earthquake tomography, *Journal of Geophysical Research-Solid Earth, 104*(B5), 10775-10786, doi: 10.1029/1999JB900036.

Mullineaux, D. R. (1996), Pre-1980 tephra-fall deposits erupted from Mount St. Helens, Washington, *U. S. Geol. Surv. Prof. Pap., 1563*.

Obrebski, M., G. A. Abers, and A. Foster (2015), Magmatic arc structure around Mount Rainier, WA, from the joint inversion of receiver functions and surface wave dispersion, *Geochemistry Geophysics Geosystems, 16*(1), 178-194, doi: 10.1002/2014GC005581.

Pallister, J. S., C. R. Thornber, K. V. Cashman, M. A. Clynne, H. Lowers, C. W. Mandeville, I. K. Brownfield, and G. P. Meeker (2008), Petrology of the 2004-2006 Mount St. Helens lava dome -- implications for magmatic plumbing and eruption triggering: Chapter 30 in A volcano rekindled: the renewed eruption of Mount St. Helens, 2004-2006; edited by D. R. Sherrod, W. E. Scott, and P. H. Stauffer, *U. S. Geol. Surv. Prof. Pap., 1750*, 647-702.

Parsons, T., R. E. Wells, M. A. Fisher, E. Flueh, and U. S. ten Brink (1999), Three-dimensional velocity structure of Siletzia and other accreted terranes in the Cascadia forearc of Washington, *Journal of Geophysical Research-Solid Earth, 104*(B8), 18015-18039, doi: 10.1029/1999JB900106.

Phillips, W. M. (1987), Geologic map of the Mount St. Helens quadrangle, Washington and Oregon: Washington Division of Geology and Earth Resources Open File Report 87-4, *1:100,000*, 1 sheet-63 p.

Porritt, R. W., R. M. Allen, D. C. Boyarko, and M. R. Brudzinski (2011), Investigation of Cascadia segmentation with ambient noise tomography, *Earth Planet. Sci. Lett., 309*(1-2), 67-76, doi: 10.1016/j.epsl.2011.06.026.

Preston, L., K. Creager, R. Crosson, T. Brocher, and A. Trehu (2003), Intraslab earthquakes: Dehydration of the Cascadia slab, *Science, 302*(5648), 1197-1200, doi: 10.1126/science.1090751.

Riddihough, R. (1984), Recent movements of the Juan de Fuca plate system, *Journal of Geophysical Research, 89*(NB8), 6980-6994, doi: 10.1029/JB089iB08p06980.

Robert, M., A. I. Qamar, R. W. King, W. Ray, K. Giorgi, C. A. Williams, C. W. Stevens, J. J. Vollick, and P. C. Zwick (2007), Fault locking, block rotation and crustal deformation in the Pacific Northwest, *Geophysical Journal International, 169*(3), 1315-1340, doi: 10.1111/j.1365-246X.2007.03371.x.

Rogers, G. and H. Dragert (2003), Episodic tremor and slip on the Cascadia subduction zone: The chatter of silent slip, *Science, 300*(5627), 1942-1943, doi: 10.1126/science.1084783.

Rubinstein, J. L., M. La Rocca, J. E. Vidale, K. C. Creager, and A. G. Wech (2008), Tidal modulation of nonvolcanic tremor, *Science, 319*(5860), 186-189, doi: 10.1126/science.1150558.

Rubinstein, J. L., J. E. Vidale, J. Gomberg, P. Bodin, K. C. Creager, and S. D. Malone (2007), Non-volcanic tremor driven by large transient shear stresses, *Nature, 448*(7153), 579-582, doi: 10.1038/nature06017.

Schasse, H. W. (1987), Geologic map of the Centralia quadrangle, Washington: Washington Division of Geology and Earth Resources Open File Report 87-11, *1:100,000*, 1 pl.-27 p.

Schmandt, B. and E. Humphreys (2011), Seismically imaged relict slab from the 55 Ma Siletzia accretion to the northwest United States, *Geology, 39*(2), 175-178, doi: 10.1130/G31558.1.

Schmidt, D. A. and H. Gao (2010), Source parameters and time-dependent slip distributions of slow slip events on the Cascadia subduction zone from 1998 to 2008, *Journal of Geophysical Research-Solid Earth, 115*, B00A18, doi: 10.1029/2008JB006045.

Shibazaki, B., K. Obara, T. Matsuzawa, and H. Hirose (2012), Modeling of slow slip events along the deep subduction zone in the Kii Peninsula and Tokai regions, southwest Japan, *Journal of Geophysical Research-Solid Earth, 117*, B06311, doi: 10.1029/2011JB009083.

Smith, J. G. (1993), Geologic map of upper Eocene to Holocene volcanic and related rocks in the Cascade Range, Washington, *U. S. Geol. Surv. Miscellaneous Investigations Map I-2005*, 20.

Snavely, P. D., N. S. MacLeod, and H. C. Wagner (1968), Tholeiitic and alkalic basalts of the Eocene Siletz River Volcanics, Oregon Coast Range, *Am. J. Sci., 266*(6), 454-481.

Spakman, W. and G. Nolet (1988), Imaging algorithms, accuracy and resolution in delay time tomography. In N. J. Vlaar, G. Nolet, M. J. R. Wortel, & S. A. P. Cloetingh (Eds.), Mathematical geophysics: A survey of recent developments in seismology and geodynamics, 155-187.

Stanley, W. D., S. Y. Johnson, and V. F. Nuccio (1994), Analysis of deep seismic reflection and other data from the southern Washington Cascades, *U. S. Geol. Surv. Open File Report 94-159*.

Stanley, W., C. Finn, and J. Plesha (1987), Tectonics and conductivity structures in the southern Washington Cascades, *Journal of Geophysical Research-Solid Earth and Planets, 92*(B10), 10179-10193, doi: 10.1029/JB092iB10p10179.

Stanley, W., S. Johnson, A. Qamar, C. Weaver, and J. Williams (1996), Tectonics and seismicity of the southern Washington Cascade range, *Bulletin of the Seismological Society of America, 86*(1), 1-18.

Swanson, D. A. (1992), Geologic map of the McCoy Peak Quadrangle, southern Cascade Range, Washington, *U. S. Geol. Surv. Open File Report 92-336*.

Symons, N. and R. Crosson (1997), Seismic velocity structure of the Puget Sound region from 3-D non-linear tomography, *Geophys. Res. Lett., 24*(21), 2593-2596, doi: 10.1029/97GL52692.

Thomas, T. W., J. E. Vidale, H. Houston, K. C. Creager, J. R. Sweet, and A. Ghosh (2013), Evidence for tidal triggering of high-amplitude rapid tremor reversals and tremor streaks in northern Cascadia, *Geophys. Res. Lett., 40*(16), 4254-4259, doi: 10.1002/grl.50832.

Trehu, A., I. Asudeh, T. Brocher, J. Luetgert, W. Mooney, J. Nabelek, and Y. Nakamura (1994), Crustal architecture of the Cascadia fore-arc, *Science, 266*(5183), 237-243, doi: 10.1126/science.266.5183.237.

Vidale, J. (1990), Finite-difference calculation of traveltimes in 3 dimensions, *Geophysics, 55*(5), 521-526, doi: 10.1190/1.1442863.

Wagner, L., D. W. Forsyth, M. J. Fouch, and D. E. James (2010), Detailed three-dimensional shear wave velocity structure of the northwestern United States from Rayleigh wave tomography, *Earth Planet. Sci. Lett., 299*(3-4), 273-284, doi: 10.1016/j.epsl.2010.09.005.

Waite, G. P. and S. C. Moran (2009), V-P structure of Mount St. Helens, Washington, USA, imaged with local earthquake tomography, *J. Volcanol. Geotherm. Res., 182*(1-2), 113-122, doi: 10.1016/j.jvolgeores.2009.02.009.

Wang, Y., F. Lin, B. Schmandt, and J. Farrell (2017), Ambient noise tomography across Mount St. Helens using a dense seismic array, *Journal of Geophysical Research-Solid Earth, 122*(6), 4492-4508, doi: 10.1002/2016JB013769.

Watanabe, T. (1993), Effects of water and melt on seismic velocities and their application to characterization of seismic reflectors, *Geophys. Res. Lett., 20*(24), 2933-2936, doi: 10.1029/93GL03170.

Weaver, C., W. Grant, and J. Shemeta (1987), Local crustal extension at Mount St. Helens, Washington, *Journal of Geophysical Research-Solid Earth and Planets, 92*(B10), 10170-10178, doi: 10.1029/JB092iB10p10170.

Weaver, C. and S. Smith (1983), Regional tectonic and earthquake hazard implications of a crustal fault zone in southwestern Washington, *Journal of Geophysical Research, 88*(NB12), 371-383, doi: 10.1029/JB088iB12p10371.

Wech, A. G. (2010), Interactive tremor monitoring, *Seismol. Res. Lett., 81*(4), 664-669, doi: 10.1785/gssrl.81.4.664.

Wech, A. G. and K. C. Creager (2008), Automated detection and location of Cascadia tremor, *Geophys. Res. Lett., 35*(20), L20302, doi: 10.1029/2008GL035458.

Wech, A. G. and K. C. Creager (2011), A continuum of stress, strength and slip in the Cascadia subduction zone, *Nature Geoscience, 4*(9), 624-628, doi: 10.1038/ngeo1215.

Wells, R. E. and R. W. Simpson (2001), Northward migration of the Cascadia forearc in the northwestern U.S. and implications for subduction deformation, *Earth, Planets and Space, 53*(4), 275-283, doi: 10.1186/BF03352384.

Wells, R., D. Bukry, R. Friedman, D. Pyle, R. Duncan, P. Haeussler, and J. Wooden (2014), Geologic history of Siletzia, a large igneous province in the Oregon and Washington Coast Range: Correlation to the geomagnetic polarity time scale and implications for a long-lived Yellowstone hotspot, *Geosphere, 10*(4), 692-719, doi: 10.1130/GES01018.1.

Wells, R., C. Weaver, and R. Blakely (1998), Fore-arc migration in Cascadia and its neotectonic significance, *Geology, 26*(8), 759-762, doi: 10.1130/0091-7613(1998)026<0759:FAMICA>2.3.CO;2.

Williams, D. L., A. Gerda, F. Carol, D. Daniel, D. J. Johnson, and D. Roger (1987), Evidence from gravity data for an intrusive complex beneath Mount St. Helens, *J. Geophys. Res., 92*, 10207-10222, doi: 10.1029/JB092iB10p10207.

Wilson, D. (1993), Confidence-intervals for motion and deformation of the Juan de Fuca plate, *Journal of Geophysical Research-Solid Earth, 98*(B9), 16053-16071, doi: 10.1029/93JB01227.

Yabe, S., A. S. Baltay, S. Ide, and G. C. Beroza (2014), Seismic-wave attenuation determined from tectonic tremor in multiple subduction zones, *Bulletin of the Seismological Society of America, 104*(4), 2043-2059, doi: 10.1785/0120140032.

Yabe, S. and S. Ide (2014), Spatial distribution of seismic energy rate of tectonic tremors in subduction zones, *Journal of Geophysical Research-Solid Earth, 119*(11), 8171-8185, doi: 10.1002/2014JB011383.

Yabe, S., Y. Tanaka, H. Houston, and S. Ide (2015), Tidal sensitivity of tectonic tremors in Nankai and Cascadia subduction zones, *Journal of Geophysical Research-Solid Earth, 120*(11), 7587-7605, doi: 10.1002/2015JB012250.

Zelt, C. (1998), Lateral velocity resolution from three-dimensional seismic refraction data, *Geophysical Journal International, 135*(3), 1101-1112, doi: 10.1046/j.1365-246X.1998.00695.x.